Graphical Abstract

Model Predictive Control for Real-Time Hybrid Testing of Multibody Dynamical Systems

Frederik Nordtorp, Vasilis Dertimanis, Giuseppe Abbiati, Eleni Chatzi

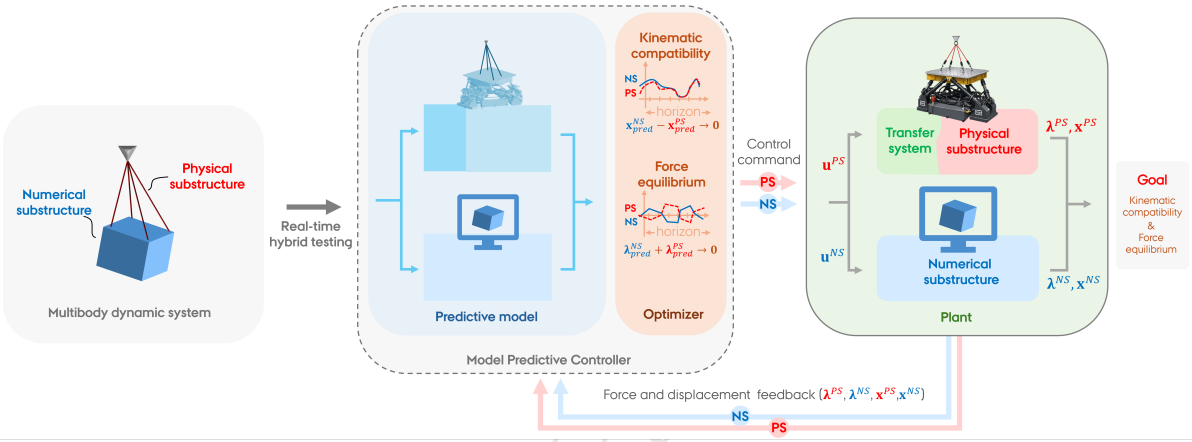

Model Predictive Control for Real-Time Hybrid Testing of Multibody Dynamical Systems

Frederik Nordtorp[a], Vasilis Dertimanis[b], Giuseppe Abbiati[a,*], Eleni Chatzi[b]

[a]*Department of Civil and Architectural Engineering, Aarhus University, Inge Lehmanns Gade 10, Aarhus, 8000, Denmark*
[b]*Institute of Structural Engineering, Department of Civil, Environmental and Geomatic Engineering, ETH Zürich, Stefano-Franscini-Platz 5, Zürich, 8093, Switzerland*

Abstract

Real-time hybrid testing provides a practical way to evaluate engineering systems under realistic operating conditions by combining numerical simulation with physical experiments. For multibody dynamical systems, however, nonlinear kinematics, coupled motion, and actuator delay make it difficult to maintain both kinematic compatibility and force equilibrium between the numerical and physical substructures. Existing model predictive control approaches for real-time hybrid testing mainly address trajectory tracking. This study proposes a model predictive control framework for real-time hybrid testing of multibody dynamical systems in which the coordination problem is formulated as a regulation problem. The framework directly targets simultaneous satisfaction of kinematic compatibility and interface force equilibrium. The general formulation is first assessed in a virtual real-time hybrid testing environment using a three-dimensional six-degree-of-freedom multibody dynamical system. The virtual results show accurate coupling, recovery of the nonlinear system response despite linearized predictive models, and robustness to moderate mismatch in the predictive model. For experimental implementation, the framework is reduced to a real-time realization with a closed-form solution. Implemented on a multi-axial simulation-table setup, the reduced controller executes in 95.6 μs, corresponding to 19.6% of the available control period at 2048 Hz, confirming real-time viability. The experiments show stable and bounded operation, satisfactory kinematic compatibility and force equilibrium, and physically consistent interaction in the presence of nonlinear and dissipative physical-substructure behavior. These results demonstrate the potential of regulation-based predictive coordination for real-time hybrid testing of nonlinear multibody dynamical systems.

Keywords: Model predictive control, Real-time hybrid testing, Multibody dynamics, Hardware-in-the-loop simulation, Delay compensation, Shake-table testing

*Corresponding author.
Email address: abbiati@cae.au.dk (Giuseppe Abbiati)

1. Introduction

1.1. Background and motivation

Experimental testing of large multibody dynamical (MBD) systems is often impractical because of system size, cost, complexity, and scaling limitations. At the same time, even high-fidelity nonlinear MBD models remain limited by modeling assumptions and by incomplete representation of physical interactions. These limitations motivate methods that combine physical experiments with numerical simulation and make MBD validation more realistic and practical.

Hybrid testing (HT) [1, 2] provides an effective framework for this purpose. In HT, an engineering system is divided into a physical substructure (PS) and a numerical substructure (NS). These substructures are coupled through kinematic compatibility and force equilibrium at their interface. When this coupling is performed in real time, the method is called real-time hybrid testing (RTHT). In many engineering fields, RTHT is also known as hardware-in-the-loop simulation [3]. Recent advances in the control of multi-actuator systems [4, 5, 6, 7] have made RTHT increasingly relevant for MBD systems. Relevant applications have been reported in wind turbines [8, 9, 10, 11], biomechanics [12], railway systems [13, 14, 15], and vehicle dynamics [16].

Real-time implementation introduces additional challenges related to the interaction between actuator dynamics and structural response. If this interaction is not handled, phase lag and effective delays appear [17, 18]. This may introduce artificial dynamics such as negative damping, which can destabilize the test and reduce both kinematic compatibility and force equilibrium at the interface. Delay-compensation methods are therefore widely used in RTHT.

Early work in this track includes the polynomial extrapolation method proposed by Horiuchi et al. [19] and its extension based on linear acceleration assumptions [20]. Carrion and Spencer [21] later extended this class of methods by introducing a model-based compensation strategy that includes structural properties and external excitation in the response prediction. A related line of work addresses substructure coupling by explicitly including actuator dynamics at the interface. Stefanaki and Sivaselvan [22, 23] introduced a framework in which the actuator is treated as a dynamic system that emulates the NS. Verma et al. [24, 25] formulated impedance matching as an optimization problem that minimizes mismatch in actuator impedance. These methods are often based on transfer-function descriptions of linearized models. Applying them to nonlinear dynamics systems, such as MBD, may therefore require additional assumptions or model extensions.

In model predictive control (MPC) [26], control inputs are computed by optimizing the predicted response of a model. Tsokanas et al. [27] proposed an MPC-based approach for RTHT in which the transfer system is controlled to track a reference trajectory generated by the NS. This trajectory-tracking formulation was later extended to account for time-varying actuation dynamics through online model adaptation [28]. Other applications of trajectory-tracking MPC in RTHT include [29].

Trajectory-tracking MPC primarily addresses the control of the transfer system by driving the actuator to follow a prescribed NS reference. Force equilibrium can, in principle, be included through additional cost terms or constraints, but the control problem remains organized around reference tracking. An alternative is to formulate the MPC problem as regulation of the interface residuals. This shifts the control objective from actuator tracking toward coupled-system coordination. Such a formulation is particularly relevant for nonlinear MBD systems, where extrapolation of the NS response may be inaccurate.

1.2. Scope

This study proposes a model predictive control framework for real-time hybrid testing of multibody dynamical systems, where the coordination between the numerical and physical substructures is formulated as a regulation problem. The proposed formulation regulates the interface by directly penalizing the kinematic compatibility and force equilibrium residuals. The general framework is first assessed in a virtual real-time hybrid testing environment. For experimental implementation, a reduced real-time realization is introduced and evaluated using a three-dimensional six-degree-of-freedom multibody dynamics system, in which the physical substructure is implemented on a multi-axial simulation table.

The remainder of the paper is organized as follows. Section 2 presents the reference case study and the experimental setup. Section 3 introduces the proposed MPC framework for RTHT, including the control formulation and predictive model. Section 4 presents the numerical validation of the framework in a virtual RTHT environment. Section 5 describes the reduced real-time experimental implementation. Section 6 presents and discusses the RTHT results. Section 7 concludes the paper.

2. Reference case study

2.1. System description

To demonstrate the proposed MPC framework and assess its ability to enforce the interface conditions, a three-dimensional hanging-mass system is used as the reference case study, as shown in Figure 1a. Although conceptually simple, the system captures key challenges of MBD systems. These include geometric nonlinearity due to large rotations and coupled translational–rotational motion. The system is partitioned into a NS and a PS. The NS consists of a rigid body with three translational degrees of freedom (longitudinal, lateral, and vertical) and three rotational degrees of freedom (roll, pitch, and yaw). The PS consists of four bungee cords mounted on a test bench, as shown in Figure 1b. The objective of the RTHT is to control the test bench so that kinematic compatibility and force equilibrium between the NS and PS are maintained in real time.

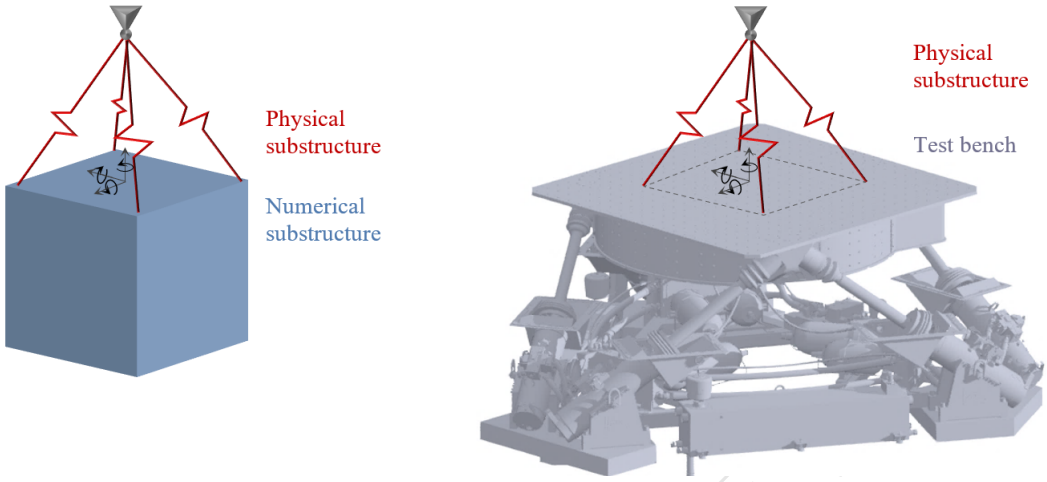

(a) (b)

Figure 1: The reference case study consists of a) the hybrid model and b) the test setup

2.2. Experimental setup

The motion of the PS is controlled using an MTS multi-axial simulation table (model 353.20 High Performance). The table is equipped with six hydraulic actuators, which provide servo-controlled longitudinal, lateral, and vertical translations, as well as space-fixed roll, pitch, and yaw rotations. The interface forces transmitted by the PS are measured using four load cells installed between the test bench and the PS. The setup is located at the IBK Structures Laboratory at ETH Zürich and is shown in Figure 2.

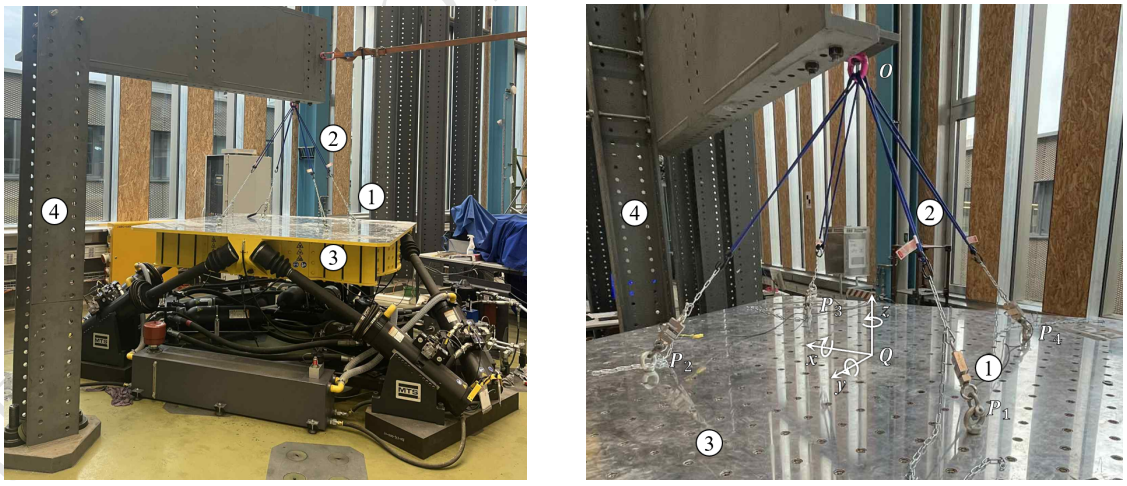

(a) (b)

Figure 2: Experimental setup showing a) the full configuration and b) a close-up view. Item 1 denotes the load cells, item 2 the bungee cords, item 3 the hexapod, and item 4 the support structure

The PS consists of four bungee cords suspended from a stiff support structure located 910 mm above the shake-table surface. The bungee cords are connected to the load

cells through adjustable metal chains, which allow the pretension to be adjusted in the initial configuration. The four load cells are arranged in a rectangular layout measuring 1000×1100 mm on the shake-table surface.

The hybrid model is implemented in Simulink and executed in real time on a Speedgoat target machine. At each control time step, the interface forces measured by the load cells are fed back to the hybrid model. These forces are used to compute updated displacement commands. All signals are sampled and exchanged at a fixed control rate of 2048 Hz. The displacement commands are applied through an internal three-variable control (TVC) loop in the MTS controller, which generates the servo-valve commands for the shake-table actuators.

Communication between the Speedgoat target and the MTS controller is established using SCRAMNet reflective memory cards. The resulting communication architecture is shown in Figure 3.

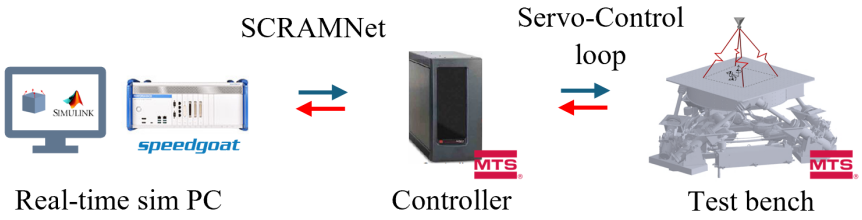

Figure 3: Communication architecture of the RTHT setup.

To derive the governing equations of the hybrid system, a hybrid MBD model is formulated using Kane's method.

2.3. Hybrid model formulation with Kane's method

In the hybrid model, the NS is evaluated numerically, while its interaction with the PS is represented through interface forces and kinematic quantities. For the MBD system considered here, the equations of motion are formulated using Kane's method [30, 31, 32]. The HT-specific assembly follows the procedure introduced in [33].

Figure 4 shows the hybrid model in its undeformed and deformed configurations.

The motion of the system is described by the generalized coordinates defined at the top of the rigid body,

$$\mathbf{q} = \begin{bmatrix} q_x & q_y & q_z & q_\phi & q_\theta & q_\psi \end{bmatrix}^T \tag{1}$$

where q_x, q_y, and q_z denote translational degrees of freedom along the global x-, y-, and z-directions, respectively. The rotational degrees of freedom q_ϕ, q_θ, and q_ψ describe the orientation of the rigid body using a space-fixed X–Y–Z Euler-angle sequence.

The Euler-angle sequence describes the orientation of a body-fixed reference frame A, defined by the orthonormal unit vectors $\hat{\mathbf{a}}_x$, $\hat{\mathbf{a}}_y$, and $\hat{\mathbf{a}}_z$, relative to the inertial reference frame N, defined by the unit vectors $\hat{\mathbf{n}}_x$, $\hat{\mathbf{n}}_y$, and $\hat{\mathbf{n}}_z$. To complete the kinematic

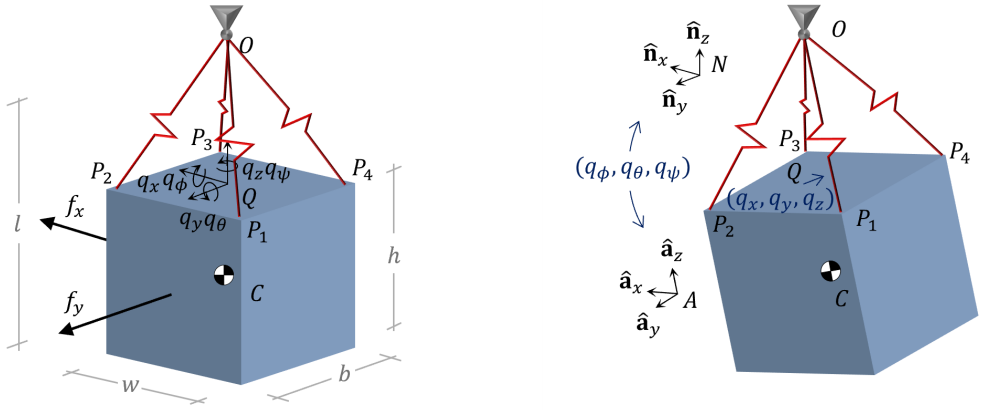

(a) (b)

Figure 4: Hybrid model in a) undeformed and b) deformed configuration

description, position vectors are introduced from a stationary reference point O to the moving points of the system. These points include the connection points P_1, P_2, P_3, and P_4, as well as the center of mass C of the rigid body. The full kinematic description used in the Kane-based derivation is provided in Appendix A.

Based on the established kinematic description, the equations of motion are derived using Kane's method. For each generalized speed, Kane's equations can be written as,

$$F_j^{NS*} + F_j^{NS} + F_j^{PS*} + F_j^{PS} = 0, \qquad j = x, y, z, \phi, \theta, \psi \tag{2}$$

where F_j^{NS} and F_j^{PS} denote the generalized active forces of the NS and PS, respectively, while F_j^{NS*} and F_j^{PS*} denote the corresponding generalized inertia forces.

2.3.1. Numerical substructure

The inertia forces and torques of the NS are defined for the rigid body attached to frame A, whose center of mass is located at point C, as

$$F_j^{NS*} = \frac{\partial^N \mathbf{v}^C}{\partial \dot{q}_j} \cdot (-m\,{}^N\mathbf{a}^C) + \frac{\partial^N \boldsymbol{\omega}^A}{\partial \dot{q}_j} \cdot (-\mathbf{I}^A \cdot {}^N\boldsymbol{\alpha}^A - {}^N\boldsymbol{\omega}^A \times (\mathbf{I}^A \cdot {}^N\boldsymbol{\omega}^A)), \quad j = x, y, z, \phi, \theta, \psi \tag{3}$$

where $\dot{q}_j$ is the time derivative to the generalized coordinate. ${}^N\mathbf{v}^C$ and ${}^N\mathbf{a}^C$ denote the velocity and acceleration of point C in frame N, respectively. Similarly, ${}^N\boldsymbol{\omega}^A$ and ${}^N\boldsymbol{\alpha}^A$ denote the angular velocity and acceleration of frame A relative to frame N. The mass of the rigid body is denoted m, and $\mathbf{I}^A$ is the inertia dyadic of the body attached to frame A,

$$\mathbf{I}^A = \frac{m}{12}(w^2 + h^2)\hat{\mathbf{a}}_x \otimes \hat{\mathbf{a}}_x + \frac{m}{12}(b^2 + h^2)\hat{\mathbf{a}}_y \otimes \hat{\mathbf{a}}_y + \frac{m}{12}(b^2 + w^2)\hat{\mathbf{a}}_z \otimes \hat{\mathbf{a}}_z \tag{4}$$

where $\otimes$ denotes the outer product.

The generalized active forces acting on the NS is assembled as,

$$F_j^{NS} = \frac{\partial^N \mathbf{v}^C}{\partial \dot{q}_j} \cdot (f_x(t)\hat{\mathbf{n}}_x + f_y(t)\hat{\mathbf{n}}_y - gm\hat{\mathbf{n}}_z - c_t {}^N\mathbf{v}^C) + \frac{\partial^N \boldsymbol{\omega}^A}{\partial \dot{q}_j} \cdot (-k_\psi q_\psi \hat{\mathbf{a}}_z - c_r {}^N\boldsymbol{\omega}^A), \quad j = x, y, z, \phi, \theta, \psi \tag{5}$$

where $g = 9.81$ m/s^2 is the gravitational acceleration, $m = 550$ kg is the mass of the rigid body, $c_t = 300N/(m/s)$ and $c_r = 30Nm/(rad/s)$ are the coefficients of added translational and rotational damping, respectively, and $k_\psi = 800Nm/rad$ is the coefficient of added rotational stiffness in the yaw direction. The time-varying external loads are defined as $f_x(t) = 300\,\Gamma(t)$ and $f_y(t) = 150\,\Gamma(t)$, where $\Gamma(t)$ is a smooth pulse-shaped modulation function centered at $t = 2\,$s.

2.3.2. Physical substructure and its predictive model

For the PS, the governing dynamics are not available in closed form, since the response is generated by the transfer system and the experimental setup. Their combined effect is therefore represented by the black-box relation,

$$F_j^{PS*} + F_j^{PS} = r_j(\mathbf{q}, \dot{\mathbf{q}}, \ddot{\mathbf{q}}, t), \qquad j = x, y, z, \phi, \theta, \psi \tag{6}$$

where $r_j(\mathbf{q}, \dot{\mathbf{q}}, \ddot{\mathbf{q}}, t)$ denotes the generalized force contribution from the PS and transfer system.

In the predictive model of the PS, denoted by $\widetilde{PS}$, the inertia contribution from the attached components is assumed to be negligible. The inertia generalized forces are therefore set to,

$$F_j^{\widetilde{PS}*} = 0, \qquad j = x, y, z, \phi, \theta, \psi. \tag{7}$$

The bungee cords are modeled as linearly elastic elements with an initial pretension. The corresponding generalized active forces are,

$$F_j^{\widetilde{PS}} = \sum_{i=1}^{4} \frac{\partial^N \mathbf{v}^{P_i}}{\partial \dot{q}_j} \cdot \left((k\delta_i + f_0)\hat{\boldsymbol{\ell}}_i \right), \qquad j = x, y, z, \phi, \theta, \psi \tag{8}$$

Here, f_0 is the pretension in each bungee cord, chosen to balance the gravitational load, and k is the cord stiffness. Furthermore, δ_i and $\hat{\boldsymbol{\ell}}_i$ denote the elongation and unit direction vector of the i-th bungee cord, respectively,

$$\delta_i = \|\mathbf{p}^{P_i O}\| - \ell_0, \qquad \hat{\boldsymbol{\ell}}_i = \frac{\mathbf{p}^{P_i O}}{\|\mathbf{p}^{P_i O}\|} \tag{9}$$

where ℓ_0 is the initial length of the bungee cords.

2.3.3. System partitioning

The system is partitioned into a NS and a PS, with the coupling enforced through interface-force contributions,

$$F_j^{NS*} + F_j^{NS} + F_j^{NS,int} = 0, \qquad j = x, y, z, \phi, \theta, \psi \tag{10}$$

$$F_j^{PS*} + F_j^{PS} + F_j^{PS,int} = 0, \qquad j = x, y, z, \phi, \theta, \psi \tag{11}$$

where $F_j^{NS,int}$ and $F_j^{PS,int}$ denote the generalized interface-force contributions acting on the NS and PS, respectively. These contributions are equal in magnitude and opposite in direction, that is, $F_j^{NS,int} = -F_j^{PS,int}$. They are given by,

$$F_j^{NS,int} = \sum_{i=1}^{4} \frac{\partial^N \mathbf{v}^{P_i}}{\partial \dot{q}_j} \cdot (\lambda_i^{NS} \hat{\boldsymbol{\ell}}_i^{NS}), \qquad F_j^{PS,int} = \sum_{i=1}^{4} \frac{\partial^N \mathbf{v}^{P_i}}{\partial \dot{q}_j} \cdot (\lambda_i^{PS} \hat{\boldsymbol{\ell}}_i^{PS}), \qquad j = x, y, z, \phi, \theta, \psi \tag{12}$$

where the directions of the interface forces are defined by the unit vectors,

$$\hat{\boldsymbol{\ell}}_i^{NS} = \frac{\mathbf{p}^{P_i O}}{\|\mathbf{p}^{P_i O}\|}\Big|_{\mathbf{q}^{NS}}, \qquad \hat{\boldsymbol{\ell}}_i^{PS} = \frac{\mathbf{p}^{P_i O}}{\|\mathbf{p}^{P_i O}\|}\Big|_{\mathbf{q}^{PS}}, \qquad i = 1, \ldots, 4 \tag{13}$$

The interface forces and their directions are illustrated in Figure 5.

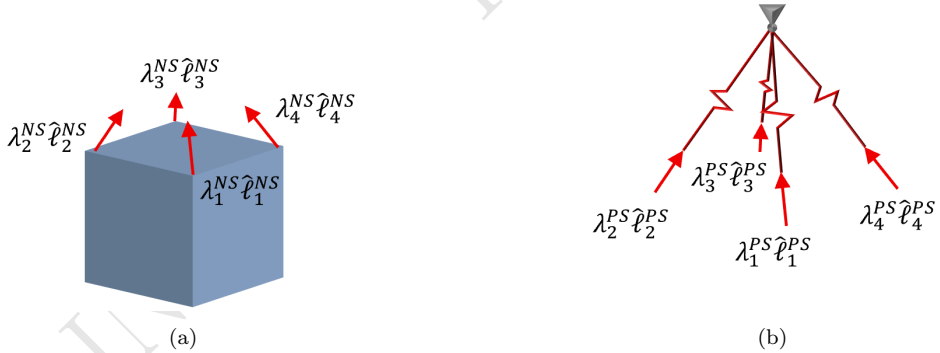

(a) (b)

Figure 5: Interface forces acting on a) the numerical substructure and b) the physical substructure

For the NS, the equation of motion is assembled from (10) as,

$$\begin{bmatrix} F_x^{NS*} + F_x^{NS} + F_x^{NS,int} \\ \vdots \\ F_\psi^{NS*} + F_\psi^{NS} + F_\psi^{NS,int} \end{bmatrix} = \mathbf{M}(\mathbf{q}^{NS})\ddot{\mathbf{q}}^{NS} + \mathbf{f}(\mathbf{q}^{NS}, \dot{\mathbf{q}}^{NS}, t) + \mathbf{J}^T(\mathbf{q}^{NS})\boldsymbol{\lambda}^{NS} = \mathbf{0} \tag{14}$$

where $\boldsymbol{\lambda}^{NS} = \begin{bmatrix} \lambda_1^{NS} & \ldots & \lambda_4^{NS} \end{bmatrix}^T$ collects the interface-force scalars. Here, $\mathbf{M}(\mathbf{q}^{NS})$ denotes the mass matrix, $\mathbf{f}(\mathbf{q}^{NS}, \dot{\mathbf{q}}^{NS}, t)$ the force vector, and $\mathbf{J}^T(\mathbf{q}^{NS})$ the Jacobian matrix that maps the interface-force directions to the generalized coordinates.

For the PS, the equations of motion are obtained from (11) as,

$$\begin{bmatrix} F_x^{PS*} + F_x^{PS} + F_x^{PS,int} \\ \vdots \\ F_\psi^{PS*} + F_\psi^{PS} + F_\psi^{PS,int} \end{bmatrix} = \mathbf{r}(\mathbf{q}^{PS}, \dot{\mathbf{q}}^{PS}, \ddot{\mathbf{q}}^{PS}, t) + \mathbf{J}^T(\mathbf{q}^{PS})\boldsymbol{\lambda}^{PS} = \mathbf{0} \tag{15}$$

Since this relation is realized experimentally, it is not available in closed form. For the MPC prediction, it is replaced by the predictive PS model, given by,

$$\begin{bmatrix} F_x^{\widetilde{PS}*} + F_x^{\widetilde{PS}} + F_x^{PS,int} \\ \vdots \\ F_\psi^{\widetilde{PS}*} + F_\psi^{\widetilde{PS}} + F_\psi^{PS,int} \end{bmatrix} = \mathbf{K}^{PS}(\mathbf{q}^{PS})\mathbf{q}^{PS} + \mathbf{J}^T(\mathbf{q}^{PS})\boldsymbol{\lambda}^{PS} = \mathbf{0} \tag{16}$$

where $\mathbf{K}^{PS}$ is the stiffness of the predictive PS model.

For physically consistent coupling of the partitioned system, the interface must satisfy kinematic compatibility and force equilibrium,

$$\mathbf{x}^{PS} - \mathbf{x}^{NS} = \mathbf{0} \tag{17}$$

$$\boldsymbol{\lambda}^{PS} + \boldsymbol{\lambda}^{NS} = \mathbf{0} \tag{18}$$

where $\mathbf{x}^{PS} = \begin{bmatrix} \mathbf{q}^{PS} \\ \dot{\mathbf{q}}^{PS} \end{bmatrix}$ and $\mathbf{x}^{NS} = \begin{bmatrix} \mathbf{q}^{NS} \\ \dot{\mathbf{q}}^{NS} \end{bmatrix}$.

In RTHT, the delay and dynamics in the transfer system can make simultaneous enforcement of these conditions challenging. An MPC-based control strategy is therefore introduced to regulate the interface mismatch.

3. Model predictive control in real-time hybrid testing

The proposed framework optimizes the inputs to the NS and PS simultaneously, with the goal of minimizing the mismatch in states and interface forces between the two substructures. This is achieved by formulating the RTHT coordination problem within a regulation-based MPC framework. Figure 6 shows a schematic overview of the framework.

Overall, the plant states $\mathbf{x}$ and interface forces $\boldsymbol{\lambda}$ are controlled through the input $\mathbf{u}$ so that the output $\mathbf{y} \to \mathbf{0}$. The control inputs are optimized over a finite prediction horizon using a predictive model of the plant, where predicted quantities are denoted by $\tilde{(\cdot)}$. Accordingly, $\tilde{\mathbf{x}}$ and $\tilde{\boldsymbol{\lambda}}$ denotes the predicted states and interface forces, given control inputs $\tilde{\mathbf{u}}$. The following subsections present the plant, the predictive model, the optimizer, and the time-stepping procedure.

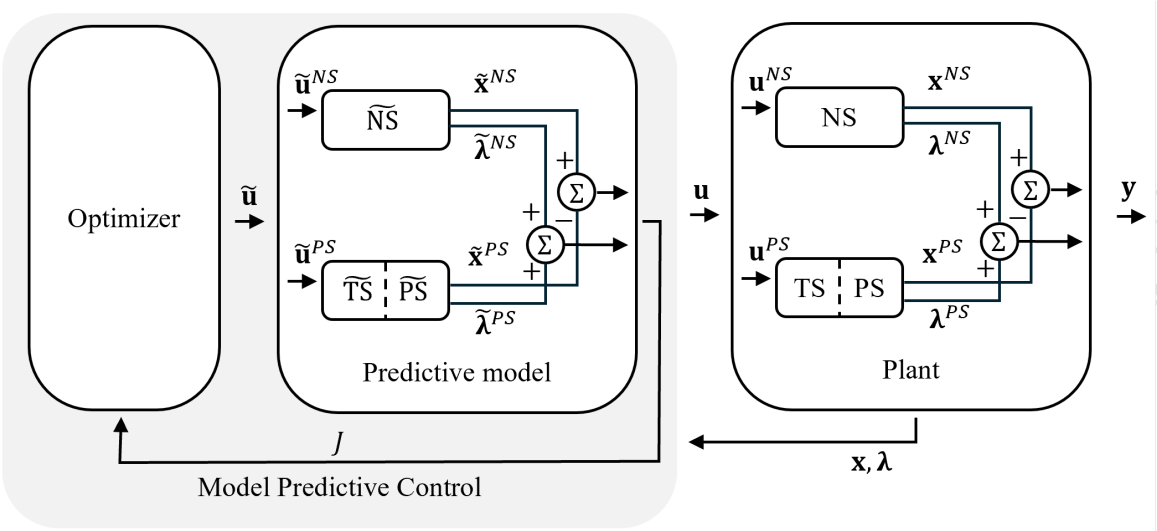

Figure 6: Schematic overview of the proposed model predictive control framework for real-time hybrid testing.

3.1. Plant

In the proposed framework, the plant consists of the coupled NS and PS. The control input is, $\mathbf{u} = \begin{bmatrix} \mathbf{u}^{PS} \\ \mathbf{u}^{NS} \end{bmatrix}$, and the objective is to regulate the output $\mathbf{y}$ such that,

$$\mathbf{y} = \begin{bmatrix} \mathbf{x}^{PS} - \mathbf{x}^{NS} \\ \boldsymbol{\lambda}^{PS} + \boldsymbol{\lambda}^{NS} \end{bmatrix} \rightarrow \mathbf{0} \tag{19}$$

where $\mathbf{x}^{PS}$ and $\mathbf{x}^{NS}$ are the state vectors of the PS and NS, respectively, and $\boldsymbol{\lambda}^{PS}$ and $\boldsymbol{\lambda}^{NS}$ are the interface forces acting on each substructure. The system is formulated in discrete time, with $t_i = i\Delta t$, where $i \in \mathbb{N}$ and Δt is the time step.

At each time step, the NS dynamics are given by,

$$\begin{aligned} \mathbf{x}_{i+1}^{NS} &= \mathbf{f}^{NS}(\mathbf{x}_i^{NS}, \boldsymbol{\lambda}_i^{NS}, \mathbf{u}_i^{NS}, t_i) \\ \boldsymbol{\lambda}_{i+1}^{NS} &= \mathbf{g}^{NS}(\mathbf{x}_i^{NS}, \boldsymbol{\lambda}_i^{NS}, \mathbf{u}_i^{NS}, t_i) \end{aligned} \tag{20}$$

where $(\cdot)_i = (\cdot)(t_i)$, and $\mathbf{f}^{NS}(\cdot)$ and $\mathbf{g}^{NS}(\cdot)$ describe the evolution of the states and interface forces, respectively. To obtain a forward dynamics formulation, the interface forces are treated as inputs, that is, $\boldsymbol{\lambda}_{i+1}^{NS} = \mathbf{u}_i^{NS}$.

Similarly, the PS dynamics are given by,

$$\begin{aligned} \mathbf{x}_{i+1}^{PS} &= \mathbf{f}^{PS}(\mathbf{x}_i^{PS}, \boldsymbol{\lambda}_i^{PS}, \mathbf{u}_i^{PS}, t_i) \\ \boldsymbol{\lambda}_{i+1}^{PS} &= \mathbf{g}^{PS}(\mathbf{x}_i^{PS}, \boldsymbol{\lambda}_i^{PS}, \mathbf{u}_i^{PS}, t_i) \end{aligned} \tag{21}$$

However, for the PS, these dynamics are not evaluated numerically. Instead, they are realized through imposed commands and measured feedback from the experimental

setup. The PS is internally controlled by the transfer system, which maps the control input $\mathbf{u}_i^{PS}$, such as displacements, accelerations, forces, or valve commands, to the physical response. The resulting states and interface forces are measured and fed back as $\mathbf{x}^{PS}$ and $\boldsymbol{\lambda}^{PS}$.

3.2. Predictive model

While the plant dynamics described above represent the true evolution of the NS and PS, they are generally nonlinear. For the PS, they are not explicitly available in analytical form and a predictive model is therefore introduced to approximate the plant behavior over a finite horizon and enable tractable optimization.

At each time step t_i, a predictive model of the plant is constructed over a finite prediction horizon. The prediction horizon is defined by the discrete instants $\tilde{t}_j = t_i + j\,\Delta\tilde{t}$ for $j = 0, \ldots, N$. Here, $\Delta\tilde{t}$ is the prediction time step, which may differ from the system time step Δt, for example $\Delta\tilde{t} = n\,\Delta t$ with $n \in \mathbb{N}$.

Over the prediction horizon, the objective function J is defined as a weighted sum of the regulation output in (19),

$$J = \sum_{j=1}^{N} \begin{bmatrix} \tilde{\mathbf{x}}_j^{PS} - \tilde{\mathbf{x}}_j^{NS} \\ \tilde{\boldsymbol{\lambda}}_j^{PS} + \tilde{\boldsymbol{\lambda}}_j^{NS} \end{bmatrix}^T \mathbf{Q} \begin{bmatrix} \tilde{\mathbf{x}}_j^{PS} - \tilde{\mathbf{x}}_j^{NS} \\ \tilde{\boldsymbol{\lambda}}_j^{PS} + \tilde{\boldsymbol{\lambda}}_j^{NS} \end{bmatrix} + \sum_{j=1}^{N-1} \begin{bmatrix} \tilde{\mathbf{u}}_j^{PS} - \tilde{\mathbf{u}}_{j-1}^{PS} \\ \tilde{\mathbf{u}}_j^{NS} - \tilde{\mathbf{u}}_{j-1}^{NS} \end{bmatrix}^T \mathbf{W} \begin{bmatrix} \tilde{\mathbf{u}}_j^{PS} - \tilde{\mathbf{u}}_{j-1}^{PS} \\ \tilde{\mathbf{u}}_j^{NS} - \tilde{\mathbf{u}}_{j-1}^{NS} \end{bmatrix} \tag{22}$$

where $\mathbf{Q}$ penalizes deviations from kinematic compatibility and force equilibrium. The matrix $\mathbf{W}$ penalizes control increments, which promotes smoother control actions.

To obtain an affine predictive model suitable for convex optimization, the NS plant dynamics from (20) are assembled and linearized around the current state,

$$\begin{bmatrix} \tilde{\mathbf{x}}_{j+1}^{NS} \\ \tilde{\boldsymbol{\lambda}}_{j+1}^{NS} \end{bmatrix} = \mathbf{A}_i^{NS} \begin{bmatrix} \tilde{\mathbf{x}}_j^{NS} \\ \tilde{\boldsymbol{\lambda}}_j^{NS} \end{bmatrix} + \mathbf{B}_i^{NS} \tilde{\mathbf{u}}_j^{NS} + \mathbf{c}_i^{NS} \tag{23}$$

where,

$$\mathbf{A}_i^{NS} = \begin{bmatrix} \frac{\partial \mathbf{f}^{NS}}{\partial \mathbf{x}^{NS}}\big|_i & \frac{\partial \mathbf{f}^{NS}}{\partial \boldsymbol{\lambda}^{NS}}\big|_i \\ \frac{\partial \mathbf{g}^{NS}}{\partial \mathbf{x}^{NS}}\big|_i & \frac{\partial \mathbf{g}^{NS}}{\partial \boldsymbol{\lambda}^{NS}}\big|_i \end{bmatrix}, \quad \mathbf{B}_i^{NS} = \begin{bmatrix} \frac{\partial \mathbf{f}^{NS}}{\partial \mathbf{u}^{NS}}\big|_i \\ \frac{\partial \mathbf{g}^{NS}}{\partial \mathbf{u}^{NS}}\big|_i \end{bmatrix}, \tag{24}$$

$$\mathbf{c}_i^{NS} = \begin{bmatrix} \mathbf{f}_i^{NS} \\ \mathbf{g}_i^{NS} \end{bmatrix} - \mathbf{A}_i^{NS} \begin{bmatrix} \mathbf{x}_i^{NS} \\ \boldsymbol{\lambda}_i^{NS} \end{bmatrix} - \mathbf{B}_i^{NS} \mathbf{u}_i^{NS} \tag{25}$$

As the PS dynamics are not available analytically, in the predictive model, they are approximated by a linear representation of the transfer system (TS) and the PS interaction. This gives,

$$\begin{bmatrix} \tilde{\mathbf{x}}_{j+1}^{PS} \\ \tilde{\boldsymbol{\lambda}}_{j+1}^{PS} \end{bmatrix} = \mathbf{A}_i^{PS} \begin{bmatrix} \tilde{\mathbf{x}}_j^{PS} \\ \tilde{\boldsymbol{\lambda}}_j^{PS} \end{bmatrix} + \mathbf{B}_i^{PS} \tilde{\mathbf{u}}_j^{PS} + \mathbf{c}_i^{PS} \tag{26}$$

Depending on the choice of control input $\tilde{\mathbf{u}}^{PS}$, the TS control primarily determines either the states $\tilde{\mathbf{x}}^{PS}$ or the interface forces $\tilde{\boldsymbol{\lambda}}^{PS}$. The remaining variables are then determined by the PS dynamics.

3.3. Optimizer

Starting from the plant state at time step t_i, the coordination problem is formulated as a finite-horizon regulation problem. The optimizer minimizes the objective function in (22), subject to the equality constraints imposed by the predictive models of the NS and PS in (23) and (26), respectively. Inequality constraints may also be included to enforce bounds on the control inputs. In that case, the optimization problem becomes,

$$
\begin{aligned}
\underset{\substack{\tilde{\mathbf{u}}_0^{PS},\ldots,\tilde{\mathbf{u}}_{N-1}^{PS},\\ \tilde{\mathbf{u}}_0^{NS},\ldots,\tilde{\mathbf{u}}_{N-1}^{NS}}}{\text{minimize}} \quad & \sum_{j=1}^{N} \begin{bmatrix} \tilde{\mathbf{x}}_j^{PS} - \tilde{\mathbf{x}}_j^{NS} \\ \tilde{\boldsymbol{\lambda}}_j^{PS} + \tilde{\boldsymbol{\lambda}}_j^{NS} \end{bmatrix}^T \mathbf{Q} \begin{bmatrix} \tilde{\mathbf{x}}_j^{PS} - \tilde{\mathbf{x}}_j^{NS} \\ \tilde{\boldsymbol{\lambda}}_j^{PS} + \tilde{\boldsymbol{\lambda}}_j^{NS} \end{bmatrix} + \sum_{j=1}^{N-1} \begin{bmatrix} \tilde{\mathbf{u}}_j^{PS} - \tilde{\mathbf{u}}_{j-1}^{PS} \\ \tilde{\mathbf{u}}_j^{NS} - \tilde{\mathbf{u}}_{j-1}^{NS} \end{bmatrix}^T \mathbf{W} \begin{bmatrix} \tilde{\mathbf{u}}_j^{PS} - \tilde{\mathbf{u}}_{j-1}^{PS} \\ \tilde{\mathbf{u}}_j^{NS} - \tilde{\mathbf{u}}_{j-1}^{NS} \end{bmatrix} \\
\text{subject to} \quad & \tilde{\mathbf{x}}_0^{PS} = \mathbf{x}_i^{PS}, \quad \tilde{\boldsymbol{\lambda}}_0^{PS} = \boldsymbol{\lambda}_i^{PS}, \quad \tilde{\mathbf{x}}_0^{NS} = \mathbf{x}_i^{NS}, \quad \tilde{\boldsymbol{\lambda}}_0^{NS} = \boldsymbol{\lambda}_i^{NS} \\
& \begin{bmatrix} \tilde{\mathbf{x}}_{j+1}^{PS} \\ \tilde{\boldsymbol{\lambda}}_{j+1}^{PS} \end{bmatrix} = \mathbf{A}_i^{PS} \begin{bmatrix} \tilde{\mathbf{x}}_j^{PS} \\ \tilde{\boldsymbol{\lambda}}_j^{PS} \end{bmatrix} + \mathbf{B}_i^{PS} \tilde{\mathbf{u}}_j^{PS} + \mathbf{c}_i^{PS}, \quad j = 0, \ldots, N-1 \\
& \begin{bmatrix} \tilde{\mathbf{x}}_{j+1}^{NS} \\ \tilde{\boldsymbol{\lambda}}_{j+1}^{NS} \end{bmatrix} = \mathbf{A}_i^{NS} \begin{bmatrix} \tilde{\mathbf{x}}_j^{NS} \\ \tilde{\boldsymbol{\lambda}}_j^{NS} \end{bmatrix} + \mathbf{B}_i^{NS} \tilde{\mathbf{u}}_j^{NS} + \mathbf{c}_i^{NS}, \quad j = 0, \ldots, N-1 \\
& \mathbf{u}_{\min}^{PS} \leq \tilde{\mathbf{u}}_j^{PS} \leq \mathbf{u}_{\max}^{PS}, \quad j = 0, \ldots, N-1 \\
& \mathbf{u}_{\min}^{NS} \leq \tilde{\mathbf{u}}_j^{NS} \leq \mathbf{u}_{\max}^{NS}, \quad j = 0, \ldots, N-1
\end{aligned}
\tag{27}
$$

The optimization yields the control sequences $\tilde{\mathbf{u}}_0^{PS}, \ldots, \tilde{\mathbf{u}}_{N-1}^{PS}$ and $\tilde{\mathbf{u}}_0^{NS}, \ldots, \tilde{\mathbf{u}}_{N-1}^{NS}$. These sequences minimize the predicted mismatch in substructure states and interface forces over the horizon. At each time step, only the first control input of the optimal sequence is applied to the plant. The optimization is then repeated using updated plant states and interface forces.

3.4. Time-stepping procedure

The MPC-based RTHT framework is implemented at each time step t_i according to the following procedure:

1. *Evaluate plant.* For the PS, measure the current state $\mathbf{x}_i^{PS}$ and interface forces $\boldsymbol{\lambda}_i^{PS}$. For the NS, compute the current state $\mathbf{x}_i^{NS}$ and interface forces $\boldsymbol{\lambda}_i^{NS}$ from (20) using the previously applied control input.

2. *Update predictive model.* Construct the predictive models of the NS and PS using the current plant states, according to (23) and (26).

3. *Optimize over the prediction horizon.* Solve the finite-horizon optimization problem in (27) to obtain the optimal control sequences $\tilde{\mathbf{u}}_0^{*PS}, \ldots, \tilde{\mathbf{u}}_{N-1}^{*PS}$ and $\tilde{\mathbf{u}}_0^{*NS}, \ldots, \tilde{\mathbf{u}}_{N-1}^{*NS}$.

4. *Apply control input.* Apply the first element of each optimal control sequence,

$$\mathbf{u}_i^{PS} = \tilde{\mathbf{u}}_0^{*PS}, \qquad \mathbf{u}_i^{NS} = \tilde{\mathbf{u}}_0^{*NS},$$

and advance to the next time step, $i = i + 1$, at wall-clock time $t = t_i + \Delta t$.

The proposed MPC-based RTHT framework is first validated in a virtual RTHT environment. It is then applied to the reference case study using a formulation adapted for real-time implementation.

4. Numerical validation

4.1. Virtual RTHT setup

For the numerical validation, the experimental setup from the reference case study is reproduced in a virtual real-time hybrid testing (vRTHT) environment. This allows controlled assessment of the proposed framework without experimental uncertainties. As in the reference case study, the input to the TS is defined in terms of displacements. The TS is modeled as a first-order lag,

$$\dot{\mathbf{q}}^{PS} = \frac{1}{\tau}(\mathbf{u}^{PS} - \mathbf{q}^{PS}) \tag{28}$$

where τ is the time constant of the actuator dynamics.

Using exact sampling [34], the continuous-time model is discretized as,

$$\tilde{\mathbf{x}}_{j+1}^{PS} = \begin{bmatrix} \tilde{\mathbf{q}}_{j+1}^{PS} \\ \tilde{\dot{\mathbf{q}}}_{j+1}^{PS} \end{bmatrix} = \begin{bmatrix} e^{-\frac{\Delta\tilde{t}}{\tau}}\tilde{\mathbf{q}}_j^{PS} + (1 - e^{-\frac{\Delta\tilde{t}}{\tau}})\tilde{\mathbf{u}}_j^{PS} \\ \frac{1}{\tau}e^{-\frac{\Delta\tilde{t}}{\tau}}(\tilde{\mathbf{u}}_j^{PS} - \tilde{\mathbf{q}}_j^{PS}) \end{bmatrix} \tag{29}$$

The predicted restoring force from the PS is updated from the equilibrium relation in (16),

$$\tilde{\boldsymbol{\lambda}}_{j+1}^{PS} = \tilde{\boldsymbol{\lambda}}_j^{PS} - (\mathbf{J}_i^{PS})^{-T}\widetilde{\mathbf{K}_i^{PS}}(\tilde{\mathbf{q}}_{j+1}^{PS} - \tilde{\mathbf{q}}_j^{PS}) \tag{30}$$

Combining (29) and (30) gives the prediction model for the coupled PS–TS dynamics in the form of (26), with,

$$\mathbf{A}_i^{PS} = \begin{bmatrix} e^{-\frac{\Delta\tilde{t}}{\tau}}\mathbf{I} & \mathbf{0} & \mathbf{0} \\ -\frac{1}{\tau}e^{-\frac{\Delta\tilde{t}}{\tau}}\mathbf{I} & \mathbf{0} & \mathbf{0} \\ (e^{-\frac{\Delta\tilde{t}}{\tau}} - 1)\mathbf{K}_i^{PS} & \mathbf{0} & \mathbf{I} \end{bmatrix}, \quad \mathbf{B}_i^{PS} = \begin{bmatrix} (1 - e^{-\frac{\Delta\tilde{t}}{\tau}})\mathbf{I} \\ \frac{1}{\tau}e^{-\frac{\Delta\tilde{t}}{\tau}}\mathbf{I} \\ (1 - e^{-\frac{\Delta\tilde{t}}{\tau}})\mathbf{K}_i^{PS} \end{bmatrix}, \quad \mathbf{c}_i^{PS} = \mathbf{0} \tag{31}$$

To obtain a forward dynamic state update for the NS, the control input is chosen as,

$$\boldsymbol{\lambda}_{i+1}^{NS} = \mathbf{u}_i^{NS} \tag{32}$$

Linearizing (14) about the state at time step i and applying a second-order Runge–Kutta scheme gives the NS prediction model in the form of (23), with,

$$\mathbf{A}_i^{NS} = \begin{bmatrix} \mathbf{I} + \Delta\tilde{t}\bar{\mathbf{A}}_i^{NS} + \frac{\Delta\tilde{t}^2}{2}\bar{\mathbf{A}}_i^{NS}\bar{\mathbf{A}}_i^{NS} & \frac{\Delta\tilde{t}}{2}\bar{\mathbf{B}}_i^{NS} + \frac{\Delta\tilde{t}^2}{2}\bar{\mathbf{A}}_i^{NS}\bar{\mathbf{B}}_i^{NS} \\ \mathbf{0} & \mathbf{0} \end{bmatrix} \tag{33}$$

$$\mathbf{B}_i^{NS} = \begin{bmatrix} \frac{\Delta\tilde{t}}{2}\bar{\mathbf{B}}_i^{NS} \\ \mathbf{I} \end{bmatrix}, \quad \mathbf{c}_i^{NS} = \begin{bmatrix} \Delta\tilde{t}\bar{\mathbf{c}}_i^{NS} + \frac{\Delta\tilde{t}^2}{2}\bar{\mathbf{A}}_i^{NS}\bar{\mathbf{c}}_i^{NS} \\ \mathbf{0} \end{bmatrix} \tag{34}$$

where,

$$\bar{\mathbf{A}}_i^{NS} = \begin{bmatrix} \mathbf{0} & \mathbf{I} \\ -\mathbf{M}_i^{NS^{-1}}\mathbf{K}_i^{NS} & -\mathbf{M}_i^{NS^{-1}}\mathbf{C}_i^{NS} \end{bmatrix}, \quad \bar{\mathbf{B}}_i^{NS} = \begin{bmatrix} \mathbf{0} \\ -\mathbf{M}_i^{NS^{-1}}\mathbf{J}_i^{NS^T} \end{bmatrix}, \quad \bar{\mathbf{c}}_i^{NS} = \begin{bmatrix} \mathbf{0} \\ -\mathbf{M}_i^{NS^{-1}}(\mathbf{f}_i^{NS} - \mathbf{K}_i^{NS}\mathbf{q}_i^{NS} - \mathbf{C}_i^{NS}\dot{\mathbf{q}}_i^{NS}) \end{bmatrix} \tag{35}$$

The virtual RTHT environment is implemented in Python. The hybrid model is derived symbolically using the *Mechanics* module of *SymPy* [35, 36]. This provides the equations of motion and their linearized forms required by the predictive model. The resulting MPC problem is then formulated and solved using `gurobipy`.

4.2. Virtual RTHT results

The proposed MPC-based RTHT framework is evaluated in a virtual environment where the NS, PS, and TS dynamics are modeled explicitly. Unless otherwise stated, the objective-function weights are chosen as $\mathbf{Q} = 10^6\mathbf{I}$ and $\mathbf{W} = \mathbf{I}$, and the input constraints in (27) are selected sufficiently large to remain inactive. The weights were selected empirically for the present virtual RTHT case. A systematic sensitivity study is not included, and the optimal weighting may depend on the considered system.

Figure 7 shows the commanded PS displacements, $\mathbf{u}^{PS}$, together with the generalized coordinates of the NS and PS, $\mathbf{q}^{NS}$ and $\mathbf{q}^{PS}$. The corresponding interface forces are shown in Figure 8, while the kinematic-compatibility and force-equilibrium residuals are shown in Figure 9. The responses are compared with nonlinear and linearized full-system reference simulations.

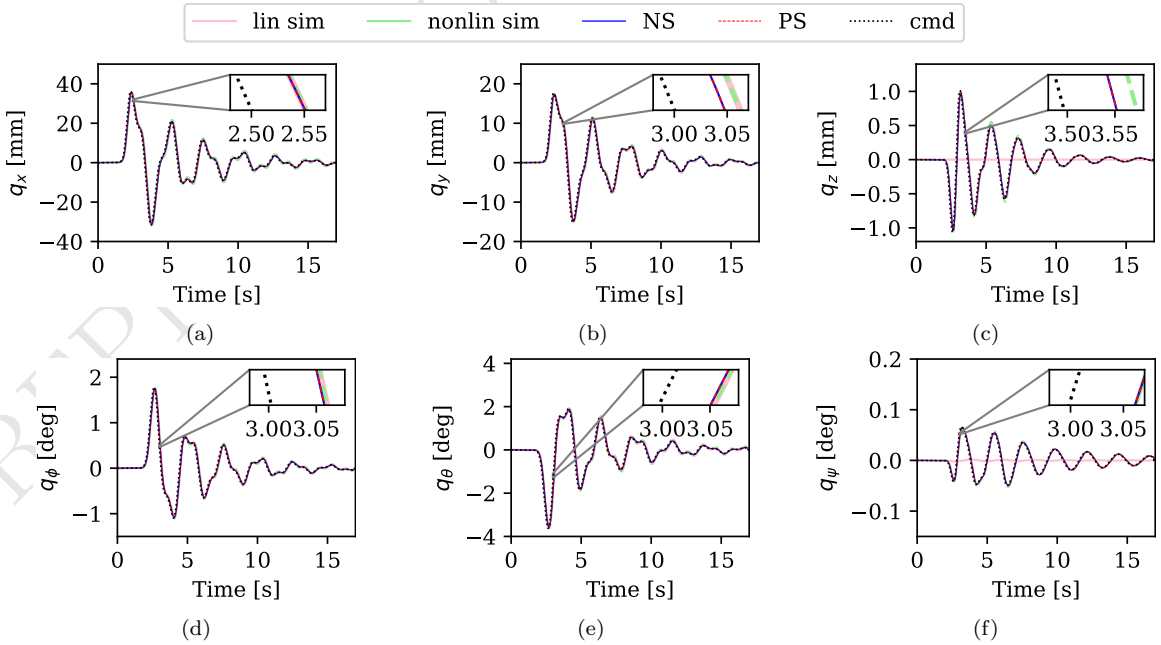

Figure 7: vRTHT state a) longitudinal, b) lateral, c) vertical, d) roll, e) pitch and f) yaw

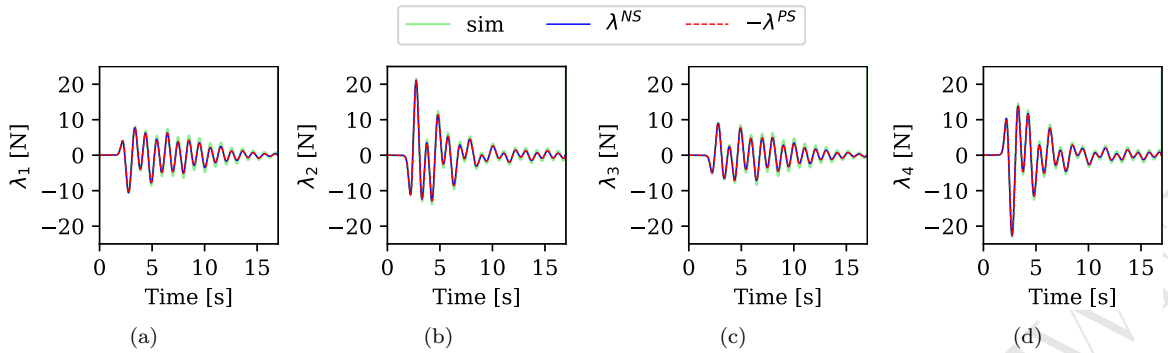

Figure 8: vRTHT interface-force responses for a) load cell 1, b) load cell 2, c) load cell 3, and d) load cell 4, showing the nonlinear reference, λ^{NS}, and $-\lambda^{PS}$

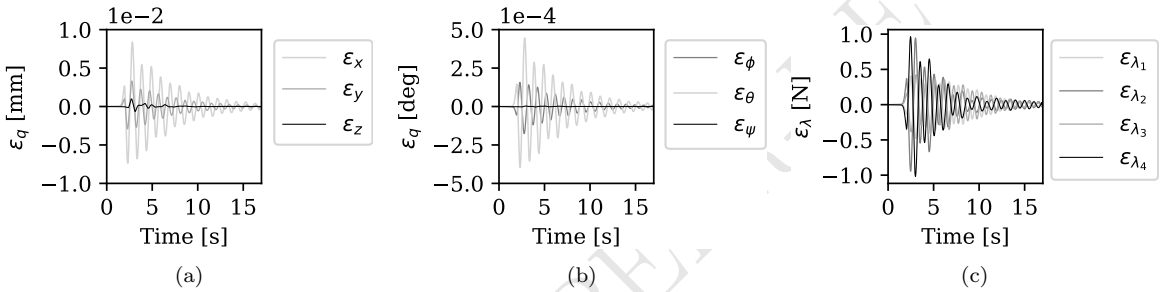

Figure 9: vRTHT mismatch in kinematic compatibility for a) translational and b) rotational dofs, and c) mismatch in force equilibrium between NS and PS. Here displacement compatibility and force equilibrium mismatches are denoted $\boldsymbol{\varepsilon}_q = \mathbf{q}^{PS} - \mathbf{q}^{NS}$ and $\boldsymbol{\varepsilon}_\lambda = \boldsymbol{\lambda}^{PS} + \boldsymbol{\lambda}^{NS}$.

Figures 7 and 8 show that kinematic compatibility and force equilibrium between the NS and PS are maintained with high accuracy throughout the simulation. The displacement responses of the two substructures are nearly indistinguishable. The interface forces remain equal and opposite over time. This indicates that the predictive model captures the coupled dynamics with sufficient accuracy over the prediction horizon. It also shows that the MPC formulation provides feasible and effective control inputs.

Figure 9 confirms this by showing the residual mismatch in kinematic compatibility and force equilibrium. For both translational and rotational coordinates, the mismatch remains close to zero throughout the simulation. The force equilibrium error is also negligible. These results show that the proposed coordination strategy maintains accurate coupling between the two substructures over time.

The influence of system nonlinearities is seen in the difference between the nonlinear and linear reference solutions. These effects are mostly seen in the vertical translation and yaw rotation, shown in Figures 7c and 7f, respectively. In these cases, no external loads are applied, and the response is governed mainly by coupling between the degrees of freedom. The RTHT responses of the NS and PS closely follow the nonlinear reference, while clear differences remain relative to the linearized model. This shows

that, although the predictive model is based on linearization, the proposed coordination framework preserves the nonlinear behavior of the system.

The coordination error is quantified using the performance indices J_1–J_3, adapted from the real-time hybrid simulation criteria proposed by Silva et al. [5].

$$J_1 = \arg\max_k \left(\sum_i \mathbf{q}_i^{NS} \mathbf{q}_{i-k}^{PS}\right) \tag{36}$$

$$J_2 = \sqrt{\frac{\sum_{i=1}^{N} [\mathbf{q}_i^{NS} - \mathbf{q}_i^{PS}]^2}{\sum_{i=1}^{N} [\mathbf{q}_i^{NS}]^2}} \times 100\% \tag{37}$$

$$J_3 = \sqrt{\frac{\sum_{i=1}^{N} [\boldsymbol{\lambda}_i^{NS} + \boldsymbol{\lambda}_i^{PS}]^2}{\sum_{i=1}^{N} [\boldsymbol{\lambda}_i^{NS}]^2}} \times 100\% \tag{38}$$

The resulting values are summarized in Table 1 and 2.

Table 1: Displacement compatibility error quantifiers for vRTHT

	Longitudinal	Lateral	Vertical	Roll	Pitch	Yaw	Overall
$J_1[-]$	0	0	0	0	0	0	0
$J_2[\%]$	0.024	0.018	0.057	0.012	0.014	0.004	0.017

Table 2: Force equilibrium error quantifiers for vRTHT

	Int. force 1	Int. force 2	Int. force 3	Int. force 4	Overall
$J_3[\%]$	0.009	0.013	0.008	0.013	0.011

The values in Table 1 and 2 confirm the performance of the proposed MPC framework in the virtual RTHT environment. The zero values of J_1 show that delay effects are compensated effectively. The very small values of J_2 and J_3 indicate negligible mismatch in kinematic compatibility and force equilibrium throughout the simulation. This level of accuracy is expected because the predictive model closely matches the plant dynamics. The present case therefore serves as an idealized baseline for the subsequent analysis of mismatch in the TS and PS predictive models.

4.3. Effect of mismatch in the predictive model

The performance of the proposed MPC framework depends on the accuracy of the predictive model, which includes both the transfer-system dynamics and the PS behavior. To assess the sensitivity of the framework to modeling errors, mismatches in both components are considered.

Figure 10 compares the case in which the delay used in the predictive model, τ_{model}, matches the plant delay τ_{plant}, with cases in which the delay is under- or overestimated.

Figure 11 compares the baseline case with cases in which the PS stiffness in the predictive model, k_{model}, is under- or overestimated relative to the plant stiffness, k_{plant}.

For both types of mismatch, a quantitative comparison with the baseline is provided in Table 3.

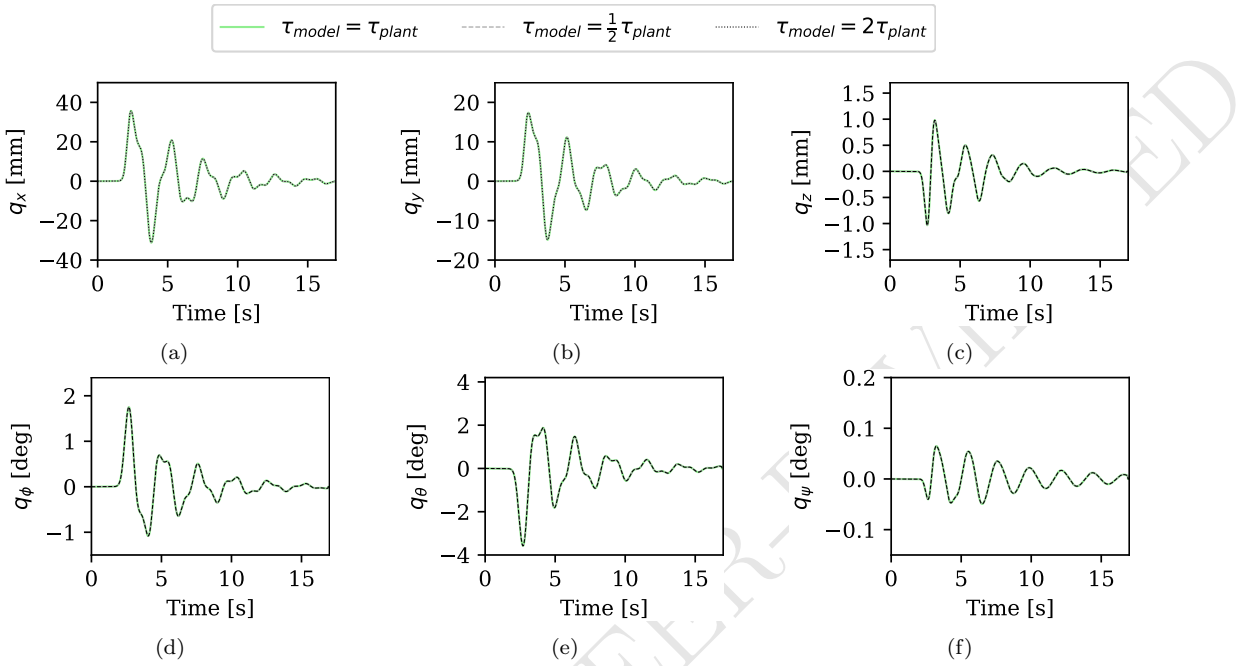

Figure 10: Influence of prediction delay on the response in a) longitudinal, b) lateral, c) vertical, d) roll, e) pitch, and f) yaw

Table 3: Error quantifiers for the baseline case and for under- and overestimation of the PS stiffness k and TS delay τ in the predictive model.

	Baseline	$k_{\text{model}} = \frac{1}{2}\,k_{\text{plant}}$	$k_{\text{model}} = 2\,k_{\text{plant}}$	$\tau_{\text{model}} = \frac{1}{2}\,\tau_{\text{plant}}$	$\tau_{\text{model}} = 2\,\tau_{\text{plant}}$
$J_1[-]$	0	0	0	1	0
$J_2[\%]$	0.017	0.319	0.207	2.321	1.353
$J_3[\%]$	0.011	0.020	0.006	0.018	0.010

The results in Figure 10 show that mismatch in the predicted TS delay has a limited effect on the overall state response. However, the error quantifiers in Table 3 show a clearer effect on the kinematic alignment between the NS and PS. This is consistent with the role of delay in the coupling loop. An incorrect delay estimate mainly shifts the timing between the commanded and realized interface motion. The NS and PS can therefore follow similar trajectories while still being slightly misaligned at the interface. Thus, TS-delay mismatch primarily affects compatibility.

In contrast, Figure 11 shows that inaccuracies in the PS model affect the response amplitude more directly. This can be attributed to the role of the PS stiffness in the prediction model. If the stiffness is inaccurate, the predicted restoring force is also inaccurate for a given interface displacement. This affects the predicted energy exchange between the NS and PS. Overestimating the stiffness increases the oscillations,

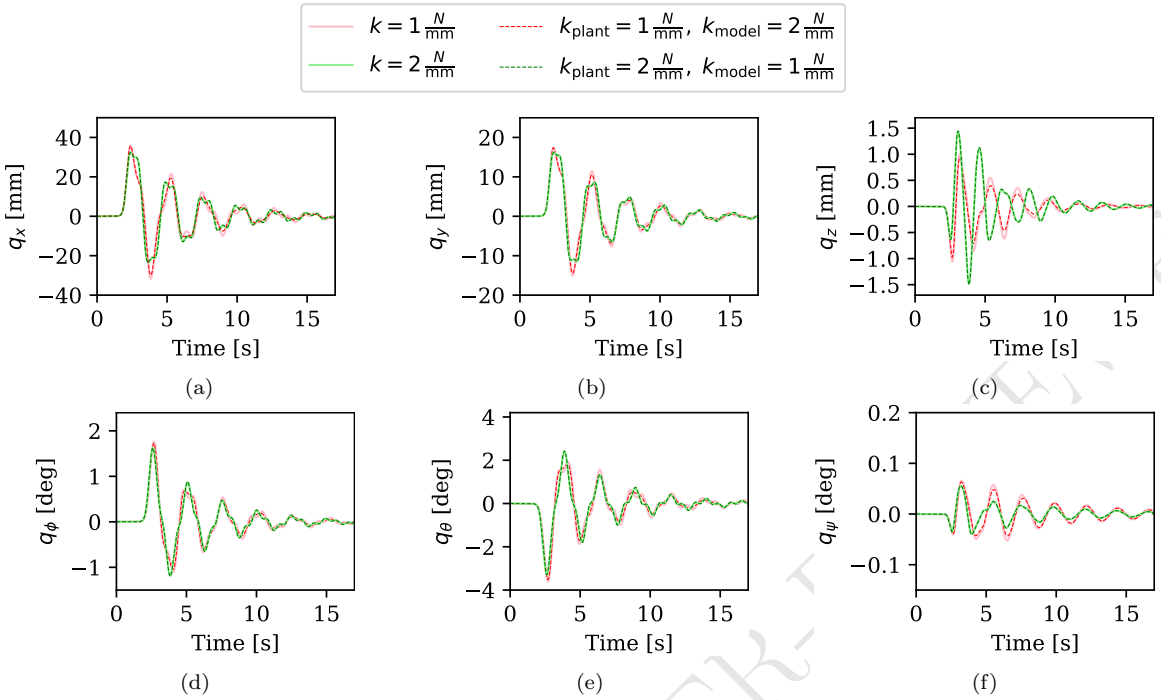

Figure 11: Influence of PS-stiffness mismatch on the vRTHT response in a) longitudinal, b) lateral, c) vertical, d) roll, e) pitch, and f) yaw

whereas underestimating it reduces them, indicating slight artificial negative and positive damping, respectively. Despite this effect, both cases remain closer to the plant behavior than to the predictive model.

These results indicate that TS-delay mismatch mainly introduces timing errors at the interface, whereas PS-stiffness mismatch changes the predicted force response. Even so, the framework remains stable and the response stays governed by the plant in all cases considered.

5. Real-time hybrid test implementation

5.1. Identification of delay

The nominal delay used in the predictive model is identified from open-loop transfer-system tests, in which prescribed displacement commands are sent directly to the test bench and the resulting motion is measured. The load-cell signals were conditioned using a digital Chebyshev type II low-pass filter designed at a sampling rate of 2048 Hz, with passband and stopband edge frequencies of 20 Hz and 30 Hz, respectively, in order to attenuate 50 Hz mains interference. The displacement measurements were conditioned in the same way, so that the delay identification is based on the filtered displacement signal supplied to the controller.

For each controlled degree of freedom, the delay is estimated as the lag maximizing the cross-correlation between the commanded and filtered displacement signals. Fig-

ure 12 shows the corresponding responses, and Table 4 summarizes the identified lag values.

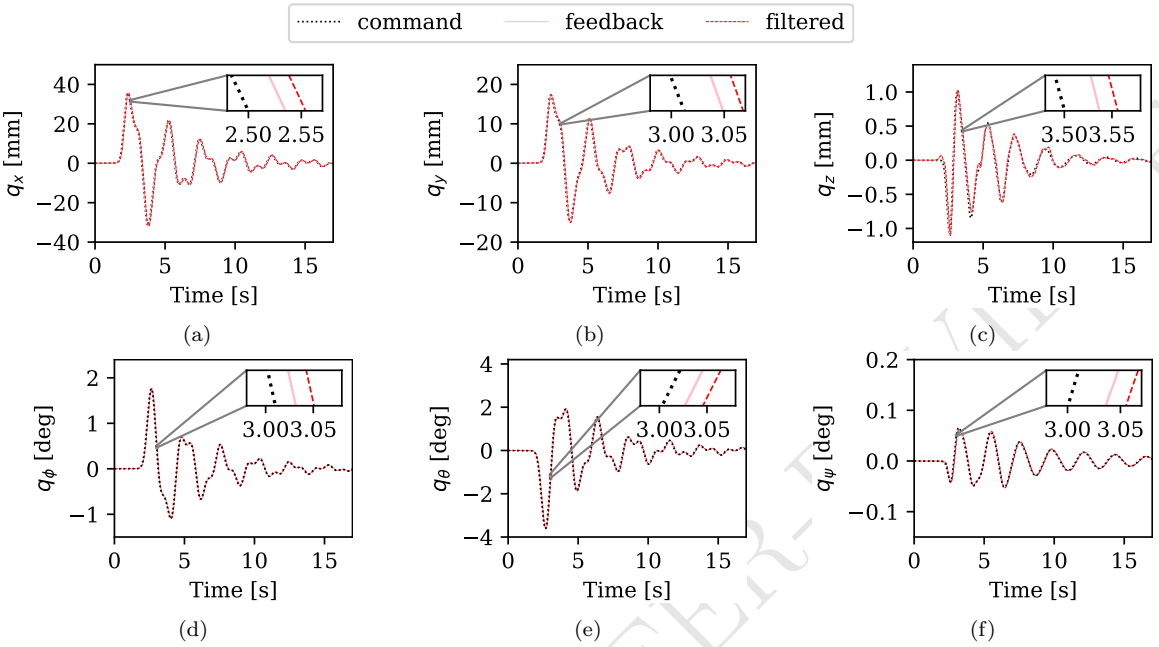

Figure 12: Open-loop transfer-system responses for the six controlled degrees of freedom: a) longitudinal, b) lateral, c) vertical, d) roll, e) pitch, and f) yaw. The commanded, measured, and filtered signals are shown together with zoomed views of the response. The nominal delay used in the reduced predictive model is identified from the lag between the commanded and filtered signals.

Table 4: Identified transfer-system delay from open-loop tests

	Longitudinal	Lateral	Vertical	Roll	Pitch	Yaw	Average
Lag [-]	103	97	92	84	89	90	92.5
τ [ms]	50.29	47.36	44.92	41.02	43.46	43.95	45.17

The identified delays range from 84 to 103 control steps (41.0–50.3 ms), with an average of 92.5 (45.17 ms). A nominal value of $n = 92$ control steps, corresponding to $\tau \approx 44.9$ ms, is therefore adopted in the reduced predictive model. Although the open-loop responses also reflect transfer-system dynamics beyond a pure delay, a nominal delay model is retained as an approximation of the dominant timing effect. The identified delay is included in the predictive model used for the Simulink implementation described next.

5.2. Implementation in Simulink

The MPC framework presented in Section 3 was implemented in Simulink for the experimental validation. At each sampling instant i, the linearized model matrices $\mathbf{A}_i$, $\mathbf{B}_i$, and $\mathbf{c}_i$ are held constant over the prediction horizon. This makes the predicted

trajectory a linear function of the future control inputs. When the bounds on the control inputs are not considered, the resulting quadratic MPC problem admits an analytical solution, which was implemented directly in a Simulink function block.

To obtain this solution, the predicted states and interface forces of each substructure are collected over the prediction horizon and written in a condensed prediction model,

$$\mathcal{Z}^s = \mathcal{A}_i^s \begin{bmatrix} \mathbf{x}_i^s \\ \boldsymbol{\lambda}_i^s \end{bmatrix} + \mathcal{B}_i^s \mathcal{U}^s + \mathcal{C}_i^s, \qquad s \in \{PS, NS\} \tag{39}$$

where, for a given substructure $s \in \{PS, NS\}$, $\mathcal{Z}^s$ collects the predicted states and interface forces over the prediction horizon, while $\mathcal{U}^s$ collects the corresponding future control inputs,

$$\mathcal{Z}^s = \begin{bmatrix} \tilde{\mathbf{x}}_1^s \\ \tilde{\boldsymbol{\lambda}}_1^s \\ \tilde{\mathbf{x}}_2^s \\ \tilde{\boldsymbol{\lambda}}_2^s \\ \vdots \\ \tilde{\mathbf{x}}_N^s \\ \tilde{\boldsymbol{\lambda}}_N^s \end{bmatrix}, \qquad \mathcal{U}^s = \begin{bmatrix} \tilde{\mathbf{u}}_0^s \\ \tilde{\mathbf{u}}_1^s \\ \vdots \\ \tilde{\mathbf{u}}_{N-1}^s \end{bmatrix} \tag{40}$$

The repeated model evaluations over the horizon are collected in the condensed prediction matrices $\mathcal{A}_i^s$ and $\mathcal{B}_i^s$, and in the offset vector $\mathcal{C}_i^s$, given by,

$$\mathcal{A}_i^s = \begin{bmatrix} \mathbf{A}_i^s \\ (\mathbf{A}_i^s)^2 \\ (\mathbf{A}_i^s)^3 \\ \vdots \\ (\mathbf{A}_i^s)^N \end{bmatrix}, \quad \mathcal{B}_i^s = \begin{bmatrix} \mathbf{B}_i^s & 0 & 0 & \cdots & 0 \\ \mathbf{A}_i^s \mathbf{B}_i^s & \mathbf{B}_i^s & 0 & \cdots & 0 \\ (\mathbf{A}_i^s)^2 \mathbf{B}_i^s & \mathbf{A}_i^s \mathbf{B}_i^s & \mathbf{B}_i^s & \cdots & 0 \\ \vdots & \vdots & \vdots & \ddots & \vdots \\ (\mathbf{A}_i^s)^{N-1} \mathbf{B}_i^s & (\mathbf{A}_i^s)^{N-2} \mathbf{B}_i^s & (\mathbf{A}_i^s)^{N-3} \mathbf{B}_i^s & \cdots & \mathbf{B}_i^s \end{bmatrix},$$

$$\mathcal{C}_i^s = \begin{bmatrix} \mathbf{c}_i^s \\ \mathbf{A}_i^s \mathbf{c}_i^s + \mathbf{c}_i^s \\ (\mathbf{A}_i^s)^2 \mathbf{c}_i^s + \mathbf{A}_i^s \mathbf{c}_i^s + \mathbf{c}_i^s \\ \vdots \\ \sum_{k=0}^{N-1} (\mathbf{A}_i^s)^k \mathbf{c}_i^s \end{bmatrix} \tag{41}$$

Using the condensed prediction model, the objective can be written as,

$$J = \left(\mathcal{E} \begin{bmatrix} \mathcal{Z}^{PS} \\ \mathcal{Z}^{NS} \end{bmatrix} \right)^T \mathcal{Q} \left(\mathcal{E} \begin{bmatrix} \mathcal{Z}^{PS} \\ \mathcal{Z}^{NS} \end{bmatrix} \right) + \left(\Delta \begin{bmatrix} \mathcal{U}^{PS} \\ \mathcal{U}^{NS} \end{bmatrix} \right)^T \mathcal{W} \left(\Delta \begin{bmatrix} \mathcal{U}^{PS} \\ \mathcal{U}^{NS} \end{bmatrix} \right) \tag{42}$$

where $\mathcal{E}$ is the interface residual matrix, which forms the stacked kinematic compatibility and force equilibrium residuals over the prediction horizon. The matrix Δ forms the input increments[1],

$$\mathcal{E} = \begin{bmatrix} \mathbf{I}_Z & \mathbf{S}_{\mp} \end{bmatrix}, \qquad \mathbf{S}_{\mp} = \mathbf{I}_N \otimes \begin{bmatrix} -\mathbf{I}_x & 0 \\ 0 & \mathbf{I}_\lambda \end{bmatrix} \tag{43}$$

$$\Delta = \begin{bmatrix} \mathbf{D}_N \otimes \mathbf{I}^{PS} & 0 \\ 0 & \mathbf{D}_N \otimes \mathbf{I}^{NS} \end{bmatrix}, \qquad \mathbf{D}_N = \begin{bmatrix} -1 & 1 & 0 & \cdots & 0 \\ 0 & -1 & 1 & \cdots & 0 \\ \vdots & \vdots & \ddots & \ddots & \vdots \\ 0 & 0 & \cdots & -1 & 1 \end{bmatrix} \tag{44}$$

The weighting matrices are assembled as,

$$\mathcal{Q} = \begin{bmatrix} \mathbf{Q} & \dots & \mathbf{0} \\ \vdots & \ddots & \vdots \\ \mathbf{0} & \dots & \mathbf{Q} \end{bmatrix}, \quad \mathcal{W} = \begin{bmatrix} \mathbf{W} & \dots & \mathbf{0} \\ \vdots & \ddots & \vdots \\ \mathbf{0} & \dots & \mathbf{W} \end{bmatrix} \tag{45}$$

Here the optimal input sequence is obtained from by solving $\partial J / \partial \begin{bmatrix} \mathcal{U}^{PS} \\ \mathcal{U}^{NS} \end{bmatrix} = \mathbf{0}$. The solution reads,

$$\begin{aligned} \begin{bmatrix} \mathcal{U}^{PS} \\ \mathcal{U}^{NS} \end{bmatrix}^\star = -\Bigg(\begin{bmatrix} \mathcal{B}_i^{PS} & \mathbf{0} \\ \mathbf{0} & \mathcal{B}_i^{NS} \end{bmatrix}^T \mathcal{E}^T \mathcal{Q} \mathcal{E} \begin{bmatrix} \mathcal{B}_i^{PS} & \mathbf{0} \\ \mathbf{0} & \mathcal{B}_i^{NS} \end{bmatrix} + \Delta^T \mathcal{W} \Delta \Bigg)^{-1} \\ \begin{bmatrix} \mathcal{B}_i^{PS} & \mathbf{0} \\ \mathbf{0} & \mathcal{B}_i^{NS} \end{bmatrix}^T \mathcal{E}^T \mathcal{Q} \mathcal{E} \left(\begin{bmatrix} \mathcal{A}_i^{PS} & \mathbf{0} \\ \mathbf{0} & \mathcal{A}_i^{NS} \end{bmatrix} \begin{bmatrix} \mathbf{x}_i^{PS} \\ \boldsymbol{\lambda}_i^{PS} \\ \mathbf{x}_i^{NS} \\ \boldsymbol{\lambda}_i^{NS} \end{bmatrix} + \begin{bmatrix} \mathcal{C}_i^{PS} \\ \mathcal{C}_i^{NS} \end{bmatrix} \right) \end{aligned} \tag{46}$$

The closed-form solution is well-defined when the matrix being inverted is nonsingular.

The equations of motion of the NS and the predictive model of the PS are derived symbolically in `SymPy`, following Section 2.3, and implemented in Simulink through automatic code generation. The resulting predictive models are used in the closed-form controller given in (46). For the real-time implementation, the prediction horizon is set to $N = 1$, the prediction time step is chosen as $n = 92$ control steps, and the input-increment penalty is omitted by setting $\mathbf{W} = \mathbf{0}$.

The present example is low dimensional, and the reported execution time should therefore be interpreted for this system size. At the fixed sampling rate of 2048 Hz, the available control period is 488.3 μs. The measured controller evaluation time is 95.6, μs, corresponding to 19.6% of the control period. Thus, the implementation satisfies the real-time constraint with substantial computational headroom.

[1] $\otimes$ indicates the Kronecker product.

For larger MBD systems, the main computational cost is expected to come from evaluating the predictive model and solving the optimization problem. Additional interface forces also increase the number of residuals and control variables. Real-time application to larger systems may therefore require a reduced predictive model that retains only the states and interface quantities needed for coordination.

6. Results and discussion

Figure 13 presents the RTHT results, including the motion of the two substructures and the control commands applied to the PS. Figure 14 shows the corresponding interface forces. Figure 15 shows the force–displacement hysteresis of the PS. Figure 16 shows the mismatch in kinematic compatibility and force equilibrium. Table 5 and 6 summarize the corresponding error metrics.

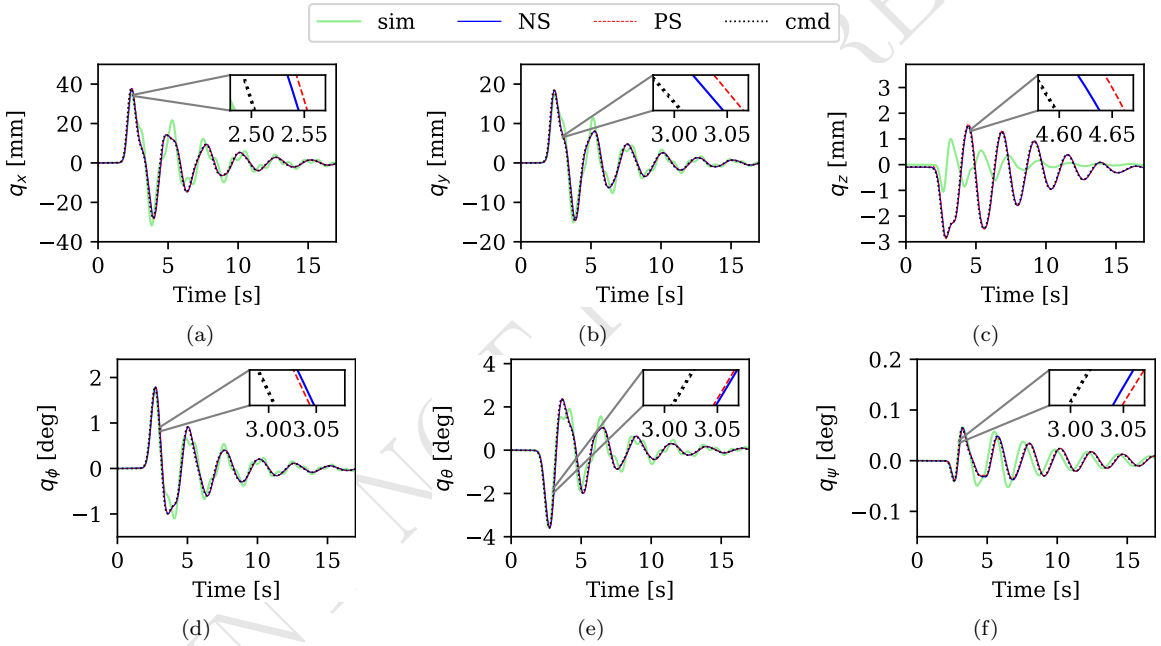

Figure 13: RTHT state responses for a) longitudinal, b) lateral, c) vertical, d) roll, e) pitch, and f) yaw motion.

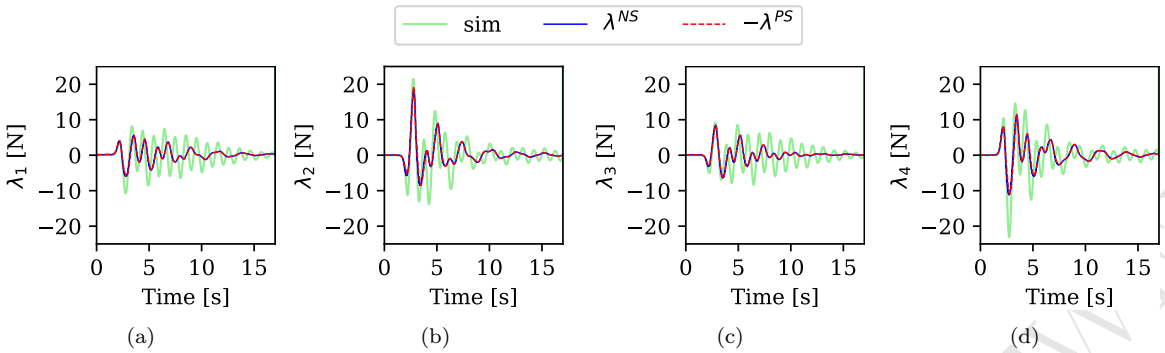

Figure 14: RTHT interface-force responses for a) load cell 1, b) load cell 2, c) load cell 3, and d) load cell 4.

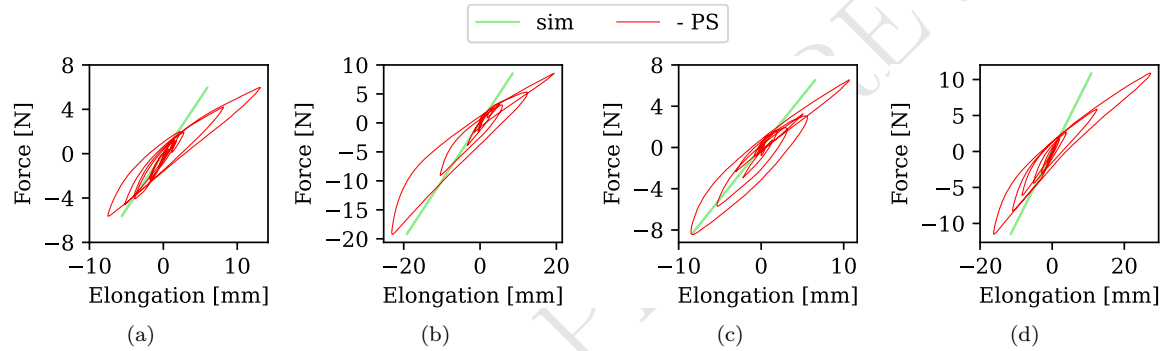

Figure 15: Force–displacement hysteresis of the physical substructure for a) load cell 1, b) load cell 2, c) load cell 3, and d) load cell 4.

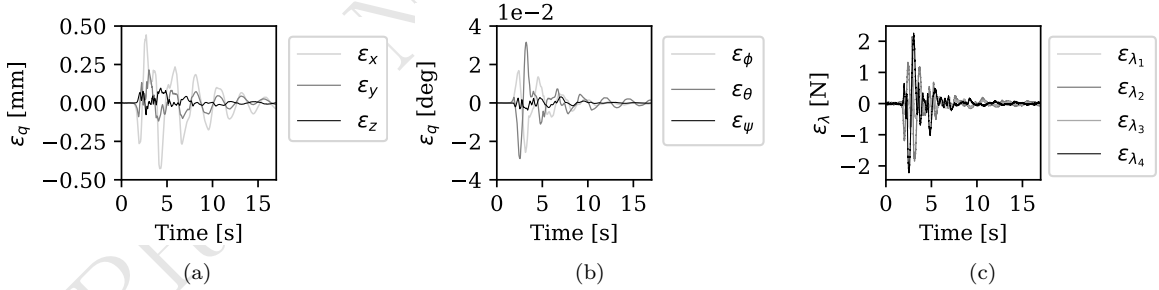

Figure 16: RTHT mismatch in displacement compatibility for a) translational and b) rotational degrees of freedom, and c) mismatch in force equilibrium between the NS and PS. Here displacement compatibility and force equilibrium mismatches are denoted $\boldsymbol{\varepsilon}_q = \mathbf{q}^{PS} - \mathbf{q}^{NS}$ and $\boldsymbol{\varepsilon}_\lambda = \boldsymbol{\lambda}^{PS} + \boldsymbol{\lambda}^{NS}$.

Table 5: Displacement compatibility error quantifiers for RTHT.

	Longitudinal	Lateral	Vertical	Roll	Pitch	Yaw	Overall
$J_1[-]$	10	4	3	-9	-4	-1	9
$J_2[\%]$	1.47	1.11	2.55	1.28	0.76	5.48	1.42

Table 6: Force equilibrium error quantifiers for RTHT.

	Int. force 1	Int. force 2	Int. force 3	Int. force 4	Overall
J_3[%]	8.72	10.94	5.88	13.99	11.26

The RTHT results remain stable and bounded throughout the test. Both displacements in Figure 13 and interface forces in Figure 14 show smooth oscillatory responses of the PS and NS in all directions, without visible growth in amplitude or loss of control. Figure 16 further shows a decreasing mismatch in the coupling conditions. This indicates that the coupling remains stable during real-time execution and does not introduce nonphysical growth in the response. The results confirm stable real-time operation of the reduced implementation and indicate consistent regulation of the coupling conditions.

The NS and PS remain reasonably well aligned throughout the RTHT. This is visible from the overlap of their trajectories in Figure 13 and the low residuals in Figure 16a and b. Additionally, the error quantifier J_2 in Table 5, remain low in all six directions, with an overall substructure-alignment error of 1.42%. This indicates that the coupling maintains good kinematic compatibility throughout the test.

In addition, the interface forces of the NS and PS remain closely balanced throughout the RTHT. This is visible in Figure 14, where the interface forces are nearly equal and opposite, and in Figure 16c, where their sum remains close to equilibrium, with a deviation of only a few Newton. The force equilibrium error remains bounded, with an overall value of $J_3 = 11.26\%$ in Table 6. This value is acceptable given the simplified transfer-system and PS predictive models, and confirms that force equilibrium is maintained at the interface throughout the test.

Regarding the fidelity of the predictive model, the simplified transfer-system model does not compensate the delay exactly in all directions. It is, however, sufficient to capture the dominant timing effect required for stable real-time coordination. In the zoomed views of Figure 13, the delayed PS feedback shows direction-dependent deviations from the NS trajectory. Table 5 quantifies this through the lag measure J_1, which ranges from -9 to 10 time steps, or -4.4 to 4.9 ms, corresponding to about 10% of the overall delay. A higher-fidelity transfer-system model could improve the alignment between the substructures, but the simplified model captures the dominant timing behavior well enough to coordinate the hybrid response. The results therefore show that exact delay compensation is not required for satisfactory RTHT performance, provided that the dominant transfer-system timing effect is represented.

Likewise, the predictive model of the PS does not need to reproduce the full physical behavior in order to support accurate coordination. Figure 15 shows that the PS bungee cords exhibit strongly nonlinear and dissipative hysteretic behavior, which is not captured by the linear prediction. This dissipative behavior is also reflected in Figure 14, where the force oscillations are more strongly damped than in the reference simulation based on the predictive model. This shows that the predictive model does not reproduce the full local response of the PS, yet the RTHT still maintains stable behavior

and satisfies the coupling objectives. The results therefore show that satisfactory RTHT performance can be achieved without a high-fidelity model, which is important for practical implementation.

7. Conclusion

This study presented a model predictive control framework for real-time hybrid testing of multibody dynamical systems. The framework is formulated as a regulation problem that directly targets kinematic compatibility and interface force equilibrium.

The general framework was first assessed in a virtual real-time hybrid testing environment. The virtual results showed accurate coupling, recovery of the nonlinear system response despite linearized predictive models, and robustness to moderate mismatch in the predictive model.

For experimental implementation, the framework was reduced to a one-step real-time realization. This reduced form uses simplified predictive models of the transfer system and the physical substructure, together with a closed-form control law. The RTHT results showed that the reduced implementation remains stable and bounded throughout the test. It maintained satisfactory kinematic compatibility and force equilibrium. It also achieved real-time execution with a controller evaluation time of 95.6 μs, corresponding to 19.6% of the available control period at 2048 Hz. The results further showed that simplified predictive models of the transfer system and the physical substructure are sufficient for satisfactory real-time coordination. Overall, the results demonstrate that the proposed MPC framework can be realized in a practical reduced form for experimental RTHT.

Future work should address more general real-time MPC implementations with longer prediction horizons, explicit constraints, and online optimization. The available computational headroom suggests that such extensions may be feasible if a numerical solver can be robustly integrated into the Simulink real-time environment.

CRediT authorship contribution statement

F. Nordtorp: Writing – review & editing, Writing – original draft, Visualization, Investigation, Formal analysis, Validation, Software, Methodology, Conceptualization. **V. Dertimanis**: Writing – review & editing, Investigation, Software, Methodology, Conceptualization. **G. Abbiati**: Writing – review & editing, Project administration, Supervision, Methodology, Conceptualization. **E. Chatzi**: Writing – review & editing, Project administration, Resources, Supervision.

Declaration of competing interest

The authors declare that they have no known competing financial interests or personal relationships that could have appeared to influence the work reported in this paper.

Acknowledgements

The authors would like to acknowledge Dr. Massimo Fiorentini (Department of Civil and Architectural Engineering at Aarhus University) and Dr. Carlo Alberto Pascucci (Rocket Lab) for the introduction to model predictive control. Mr. Dominik Werne and Mr. Andreas Reusser from the laboratory of the Institute of Structural Engineering of ETH Zürich are also acknowledged for their support in conducting the experiments presented in this work.

This research was funded by EUDP – the Energy Technology Development and Demonstration Program – through the following projects:

- Project 64019-0595 DLTE, a collaboration between Aarhus University, Department of Electrical and Computer Engineering and Department of Civil and Architectural Engineering (AU-ECE, AU-CAE), R&D Test Systems A/S, and FORCE Technology.
- Project 640222-497272 DIGIT-BENCH, a collaboration between Aarhus University, Department of Electrical and Computer Engineering and Department of Civil and Architectural Engineering (AU-ECE, AU-CAE), R&D Test Systems A/S, and Lindø Offshore Renewable Center (LORC).

Data Availability Statement

Some or all data, models, or code that support the findings of this study are available from the corresponding author upon reasonable request.

References

[1] M. Hakuno, M. Shidawara, and T. Hara, "Dynamic destructive test of a cantilever beam, controlled by an analog computer," 1969.

[2] K. Takanashi, K. Udagawa, M. Seki, T. Okada, and H. Tanaka, "Non-linear earthquake response analysis of structures by a computer-actuator on-line system," *Transaction of the Architectural Institute of Japan*, vol. 229, pp. 77–83, 03 1975.

[3] F. Mihalič, M. Truntič, and A. Hren, "Hardware-in-the-loop simulations: A historical overview of engineering challenges," *Electronics*, vol. 11, no. 15, 2022.

[4] G. Fermandois and B. F. Spencer, "Model-based framework for multi-axial real-time hybrid simulation testing," *Earthquake Engineering and Engineering Vibration*, vol. 16, no. 4, pp. 671–691, 2017.

[5] C. E. Silva, D. Gomez, A. Maghareh, S. J. Dyke, and B. F. Spencer, "Benchmark control problem for real-time hybrid simulation," *Mechanical Systems and Signal Processing*, vol. 135, p. 106381, 2020.

[6] A. Najafi, G. A. Fermandois, S. J. Dyke, and B. F. Spencer, "Hybrid simulation with multiple actuators: A state-of-the-art review," *Engineering Structures*, vol. 276, p. 115284, 2023.

[7] J. W. Condori Uribe, M. Salmeron, E. Patino, H. Montoya, S. J. Dyke, C. E. Silva, A. Maghareh, M. Najarian, and A. Montoya, "Experimental benchmark control problem for multi-axial real-time hybrid simulation," *Frontiers in Built Environment*, vol. Volume 9 - 2023, 2023.

[8] T. Sauder, V. Chabaud, M. Thys, E. E. Bachynski, and L. O. Sæther, "Real-Time Hybrid Model Testing of a Braceless Semi-Submersible Wind Turbine: Part I — The Hybrid Approach," in *Volume 6: Ocean Space Utilization; Ocean Renewable Energy*, (Busan, South Korea), p. V006T09A039, American Society of Mechanical Engineers, June 2016.

[9] M. Belloli, I. Bayati, A. Facchinetti, A. Fontanella, H. Giberti, F. La Mura, F. Taruffi, and A. Zasso, "A hybrid methodology for wind tunnel testing of floating offshore wind turbines," *Ocean Engineering*, vol. 210, p. 107592, 2020.

[10] Z. Zhang, A. Staino, B. Basu, and S. R. Nielsen, "Performance evaluation of full-scale tuned liquid dampers (tlds) for vibration control of large wind turbines using real-time hybrid testing," *Engineering Structures*, vol. 126, pp. 417–431, 2016.

[11] H. Ding, Z. Zhang, J. Wang, J. Zhang, and O. Altay, "Multiscale fluid–structure coupled real-time hybrid simulation of monopile wind turbines with vibration control devices," *Mechanical Systems and Signal Processing*, vol. 215, p. 111439, 2024.

[12] S. Herrmann, M. Kaehler, R. Souffrant, R. Rachholz, J. Zierath, D. Kluess, W. Mittelmeier, C. Woernle, and R. Bader, "Hil simulation in biomechanics: A new approach for testing total joint replacements," *Computer Methods and Programs in Biomedicine*, vol. 105, no. 2, pp. 109–119, 2012.

[13] P. Shao, W. Guo, Q. Lei, and C. Zeng, "Adaptive compound control for the real-time hybrid simulation of high-speed railway train–bridge coupling vibration," *Structural Control and Health Monitoring*, vol. 28, 07 2021.

[14] W. Guo, C. Zeng, H. Gou, Q. Gu, T. Wang, H. Zhou, B. Zhang, and J. Wu, "Real-time hybrid simulation of high-speed train-track-bridge interactions using the moving load convolution integral method," *Engineering Structures*, vol. 228, p. 111537, 2021.

[15] H. Liu, Z. Tang, and R. Enokida, "Stability prediction method of time-varying real-time hybrid testing system on vehicle-bridge coupled system," *Mechanical Systems and Signal Processing*, vol. 216, p. 111463, 2024.

[16] W. Witteveen and L. Koller, "Frf-based non-simultaneous real-time hybrid testing of multiple subsystems with moderate nonlinearities," *Mechanical Systems and Signal Processing*, vol. 188, p. 109944, 2023.

[17] X. Gao, N. Castaneda, and S. J. Dyke, "Real time hybrid simulation: from dynamic system, motion control to experimental error," *Earthquake Engineering & Structural Dynamics*, vol. 42, no. 6, pp. 815–832, 2013.

[18] S. J. Dyke, B. F. Spencer, P. Quast, and M. K. Sain, "Role of control-structure interaction in protective system design," *Journal of Engineering Mechanics*, vol. 121, no. 2, pp. 322–338, 1995.

[19] T. Horiuchi, M. Inoue, T. Konno, and Y. Namita, "Real-time hybrid experimental system with actuator delay compensation and its application to a piping system with energy absorber," *Earthquake Engineering & Structural Dynamics*, vol. 28, no. 10, pp. 1121–1141, 1999.

[20] T. Horiuchi and T. Konno, "A new method for compensating delay in time hybrid experiments," *Philosophical Transactions of The Royal Society A: Mathematical, Physical and Engineering Sciences*, vol. 359, pp. 1893–1909, 09 2001.

[21] J. Carrion and B. Spencer, "Real-time hybrid testing using model-based delay compensation," *Smart Structures and Systems*, vol. 4, 01 2006.

[22] A. Stefanaki and M. V. Sivaselvan, "A simple strategy for dynamic substructuring: I. Concept and development," *Earthquake Engineering & Structural Dynamics*, vol. 47, pp. 1801–1822, July 2018.

[23] A. Stefanaki, M. V. Sivaselvan, S. Weinreber, and M. Pitman, "A simple strategy for dynamic substructuring: II. Experimental evaluation," *Earthquake Engineering & Structural Dynamics*, vol. 47, pp. 1823–1843, July 2018.

[24] M. Verma and M. Sivaselvan, "Impedance matching control design for the benchmark problem in real-time hybrid simulation," *Mechanical Systems and Signal Processing*, vol. 134, p. 106343, Dec. 2019.

[25] M. Verma, M. V. Sivaselvan, and J. Rajasankar, "Impedance matching for dynamic substructuring," *Structural Control and Health Monitoring*, vol. 26, Nov. 2019.

[26] J. Rawlings, D. Mayne, and M. Diehl, *Model Predictive Control: Theory, Computation, and Design*. 01 2017.

[27] N. Tsokanas, D. Wagg, and B. Stojadinović, "Robust model predictive control for dynamics compensation in real-time hybrid simulation," *Frontiers in Built Environment*, vol. Volume 6 - 2020, 2020.

[28] N. Tsokanas, R. Pastorino, and B. Stojadinović, "Adaptive model predictive control for actuation dynamics compensation in real-time hybrid simulation," *Mechanism and Machine Theory*, vol. 172, p. 104817, 2022.

[29] C. Zeng, W. Guo, and P. Shao, "Performance study of model predictive control with reference prediction for real-time hybrid simulation," *Journal of Vibration and Control*, vol. 30, no. 7-8, pp. 1659–1673, 2024.

[30] T. Kane and C. Wang, "On the derivation of equations of motion," *Journal of the Society of Industrial and Applied Mechanics*, vol. 13, no. 2, pp. 487–492, 1965.

[31] A. Banerjee, *Flexible Multibody Dynamics: Efficient Formulations with Applications*. CRC Press, 2nd ed., 2022.

[32] C. Roithmayr and D. H. Hodges, *Dynamics: Theory and Application of Kane's Method*. Cambridge University Press, 2016.

[33] F. Nordtorp, E. E. Baş, C. Gomes, P. Jensen, J. Jørgensen, and G. Abbiati, "Hybrid testing of wind turbine components using Kane's method," 2026. engrXiv preprint.

[34] A. Bemporad, "Discrete-time linear systems," 2010. Online lecture notes.

[35] J. K. Moore, "Learn multibody dynamics," 2022. Accessed on January 16, 2024.

[36] SymPy Development Team, "Sympy documentation," 2023. Accessed on January 16, 2024.

Appendix A. Kinematics

(i) A frame A, with orthogonal unit vectors $\hat{\mathbf{a}}_x$, $\hat{\mathbf{a}}_y$ and $\hat{\mathbf{a}}_z$, follows the mass. The orientation of frame A with respect to the inertia frame N, described by $\hat{\mathbf{n}}_x$, $\hat{\mathbf{n}}_y$ and $\hat{\mathbf{n}}_z$, is given by the rotation matrix,

$$
{}^{N}\mathbf{C}^{A} = \begin{bmatrix} c_\theta c_\psi & c_\theta s_\psi & -s_\theta \\ -c_\phi s_\psi + s_\phi s_\theta c_\psi & c_\phi c_\psi + s_\phi s_\theta s_\psi & s_\phi c_\theta \\ s_\phi s_\psi + c_\phi s_\theta c_\psi & -s_\phi c_\psi + c_\phi s_\theta s_\psi & c_\phi c_\theta \end{bmatrix} \tag{A.1}
$$

where $c_\cdot = \cos(\cdot)$ and $s_\cdot = \sin(\cdot)$.

(ii) Position vector from point O to C

$$
\mathbf{p}^{OC} = q_x \hat{\mathbf{n}}_x + q_y \hat{\mathbf{n}}_y + (q_z - l)\hat{\mathbf{n}}_z - \frac{h}{2}\hat{\mathbf{a}}_z \tag{A.2}
$$

Position vector from point C to P_i

$$\mathbf{p}^{CP_1} = -\frac{w}{2}\hat{\mathbf{a}}_x + \frac{b}{2}\hat{\mathbf{a}}_y + \frac{h}{2}\hat{\mathbf{a}}_z, \quad \mathbf{p}^{CP_2} = \frac{w}{2}\hat{\mathbf{a}}_x + \frac{b}{2}\hat{\mathbf{a}}_y + \frac{h}{2}\hat{\mathbf{a}}_z \tag{A.3}$$

$$\mathbf{p}^{CP_3} = \frac{w}{2}\hat{\mathbf{a}}_x - \frac{b}{2}\hat{\mathbf{a}}_y + \frac{h}{2}\hat{\mathbf{a}}_z, \quad \mathbf{p}^{CP_4} = -\frac{w}{2}\hat{\mathbf{a}}_x - \frac{b}{2}\hat{\mathbf{a}}_y + \frac{h}{2}\hat{\mathbf{a}}_z \tag{A.4}$$

Appendix B. filtering effect

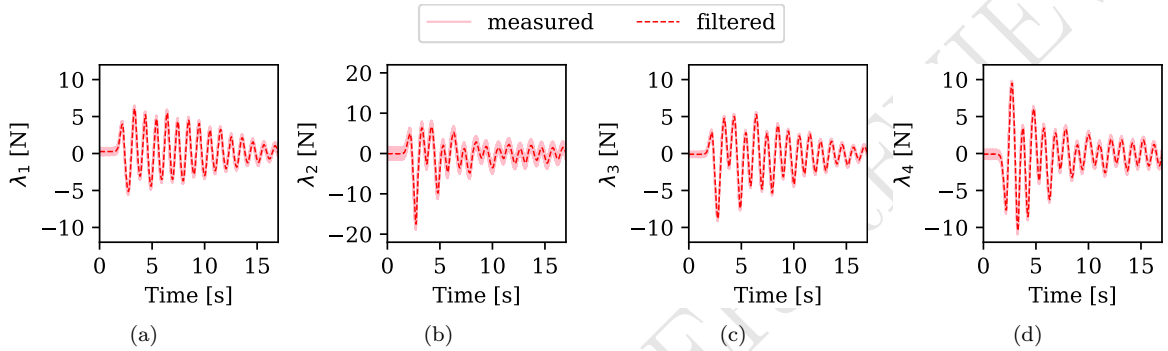

Figure B.17: Measured and filtered interface-force signals for a) load cell 1, b) load cell 2, c) load cell 3, and d) load cell 4, illustrating the effect of the real-time signal-conditioning filter used in the experimental implementation.